EUREC4A experiment: Air-Sea Flux Mast Data

Denis Bourras[1] Nicolas Geyskens[2], Gilles Reverdin[3], Aurélien Clémençon[1], Hervé Barrois[1], Hubert Branger[4], and Christopher Luneau[5]

[1]MIO, Mediterranean Institute of Oceanology, Marseille, France

[2]DT-INSU, Meudon, France

[3]LOCEAN, Paris, France

[4]IRPHE, Marseille, France

[5]OSU-Pytheas, Marseille, France

Technical report LASIF 2020-03DB

30 November 2020

Version 1.1

Figure 1. The R/V Atalante and the flux mast on the meteorological tower of the front deck

1.Introduction

This document is based on the first work by Geyskens et al. (2019), in which the instruments are described as well as the logbook and the first Figures describing the data of the flux mast. In the present document, we recall the basic instrumental setup described in Geyskens et al. (2019), next we provide a detailed comparison of meteorological data, and we estimate the air-sea turbulent fluxes. We compare the ship data to the OCARINA platform data. Last, we provide a flux dataset with error bars and we give recommendations for improving the flux mast for the future campaigns.

1.1 Flux mast location and instruments

As part of the EUREC^{4}A project (H. Bellenger, S. Speich, LMD), the "flux mast" national instrument was installed on the Reseach Vessel R/V Atalante from Genavir. The flux mast holds instruments that measure atmospheric turbulence and meteorological variables. The collected data are used to estimate the turbulent fluxes of momentum and heat at the air-sea interface. Specifically, the flux mast instruments measure air pressure, air temperature, humidity, air refraction index, CO_2, H_2O, the three components of the wind vector, and the upward and downward solar and infrared radiation fluxes. The fluxes calculated are the latent and sensible heat fluxes, the momentum (or equivalently, the friction velocity), the aerodynamic roughness height, and the Monin-Obukhov ratio, which describes the dynamic stability of the surface boundary layer.

The exact location of the flux mast is shown in Figure 1. It is also represented in Figure 2, which is a scale representation of the ship.

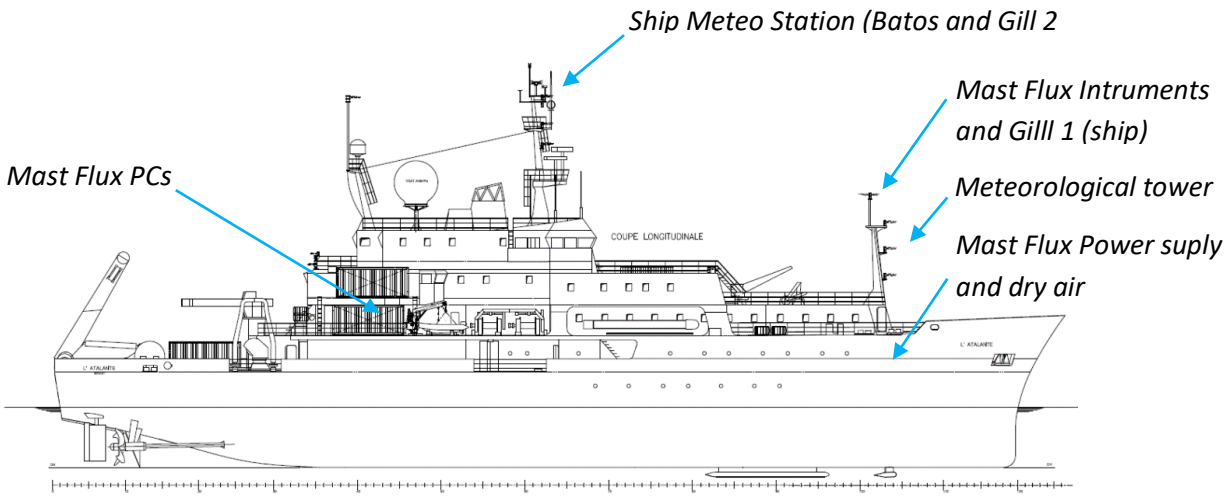

Figure 2. Side view of the R/V ATALANTE

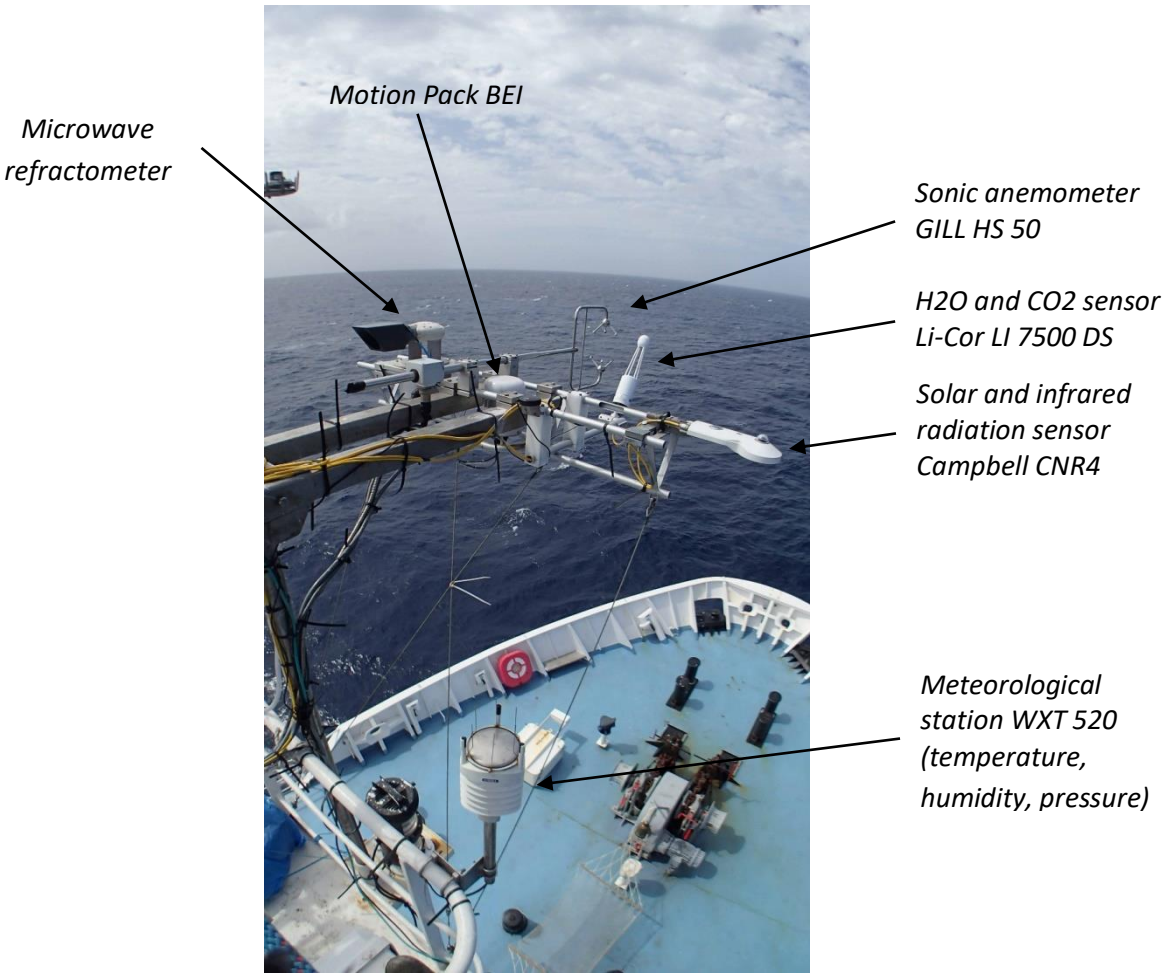

Figure 3. Instruments of the flux mast

There are six instruments on the flux mast (Figure 3), namely:

- **A prototype microwave refractometer (developed at LATMOS laboratory, see Delahaye et al., 2001)**: air refraction index, sampled at 50 Hz
- **A BEI motion pack Inertial Motion Unit**: Six degrees of freedom (three linear accelerations, three angular velocities), sampled at 50 Hz
- **A Gill HS-50 sonic anemometer**: *u*, *v*, *w* wind components, and sonic temperature, at 50 Hz
- **A Campbell Li-Cor *LI 7500 DS* instrument**: CO_2 (µmol/mol, mol/m3, absorbance), H_2O (µmol/mol, mol/m3, absorbance), dew point, at 20 Hz
- **A weather station Vaisala WXT 520**: Air temperature, relative humidity, and atmospheric pressure, wind direction, wind speed, and precipitation, at 1 Hz
- **A Campbell CNR4 pyranometer and pyrgeometer**: Upward and downward radiation fluxes (solar and infrared) at 1 Hz
- **A GPS**: position, followed route, and ship speed, at 1 Hz.

For the data processing, ancillary data are also used. They are routinely collected inboard: GPS data (position, route and speed), meteorological variables (instruments on the central mast), and the sea surface temperature.

Four persons were involved in the setup and in the data processing of the flux mast: Nicolas Geyskens (DT-INSU) was on board during the campaign, Aurélien Clémençon (DT-INSU) and Hervé

Barrois (DT-INSU) helped to set up the flux mast, and Denis Bourras (MIO) was in Marseille to process the data.

The data are acquired on two personal computers (PCs). There are several data time stamps recorded:

- On the first PC (PC-flux) :
  - Meteorological, position, and radiation data are transmitted by a Campbell CR1000 system placed on the mast, through a serial line (WXT, GPS, and CNR4) at ~1 Hz. There are gaps in the data file (data lines missing), and some entire files were lost, due to connection issues. Three types of time data are recorded for each line of data: the internal CR1000 time (not used), the PC-FLUX time, and the GPS UTC time.
  - Gill, BEI, and refractometer data are collected at ~50 Hz in two distinct data files. There are no time data recorded, thus the time is deduced from the name of the file, which contains the PC-FLUX time, plus the number of lines (normally 90 000 for a 30' file received). We noted that systematically, some lines of data were lost in the Gill/BEI files (next section).
- On the second PC (PC-Licor) :
  - Licor files were recorded at 10 Hz during the first week, then at 20 Hz. The time of the PC is recorded, at the nanosecond. Unfortunately, the PC-Licor time fluctuates and is periodically readjusted in an unpredictable manner against GPS data (see next section). Some files are missing.

1.2 Missing data and time issues

1.2.1 Gill, BEI, and refractometer data

Gill files contain sonic data (wind, temperature) plus BEI data that are acquired through dedicated input ports in the Gill data acquisition system.

Each Gill file is named as YYMMDDHHMMSS.Gill (e.g. 200122000253.Gill). The Gill files are text files that contain data lines at 50 Hz. There should be 90 000 lines per file (they are half-hour files), but some lines are systematically missing (Figure 4). One outlier (a 50 000 line-file) was omitted in Figure 4).

Figure 4. Missing number of lines in Gill-BEI files

At maximum, 6 lines are lost, which corresponds to 6/1800=0.033 seconds per half-hour. This has a negligible impact on the rest of the study, because each file is named independently from the others. More problematic is the drift of the PC-FLUX clock (see hereafter).

The refractometer files are named as YYMMDDHHMMSS.Refrac. For memory, please note that on top of each data line is a data counter, which is modulo 16 (not used here). The number of lines is well respected for each data file (90 000).

There is no good option for correcting time when there are missing lines in the Gill-BEI files. As a choice, we joined to each data line a time stamp calculated with the time of the first data) plus a time increment set to 1/50 second per line of data.

1.2.2 Issues with Licor data

Over the entire data set, the time difference between two successive measurements can reach several hours (revealing the gaps in data files, Figure 5).

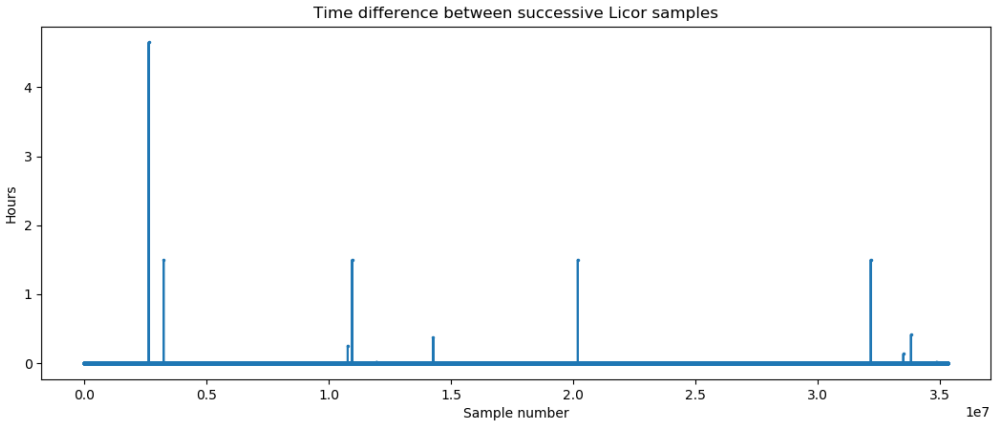

Figure 5. Gaps in Licor data

If we zoom on small time differences (Figure 6), we see that the sample rate was set from 10 Hz to 20 Hz at 1/3 of the experiment.

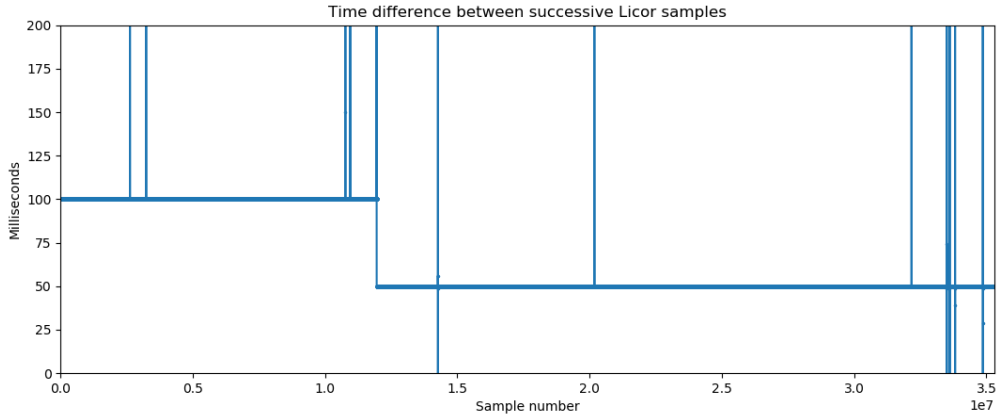

Figure 6. Zoom in Figure 5 data, between 0 and 200 ms of time difference

1.2.3 Drift of PC-FLUX clock

In the CR1000 files, the PC-FLUX time is recorded in addition to the GPS time. Thus, the difference between the two time-series can be analyzed (Figure 7). It reveals that several sequences of about 20'-30' are missing. In the details, the global trend of the time difference is negative, on the order of 4 sec per day, which sums up to 100 seconds at the end of the experiment (Figure 8).

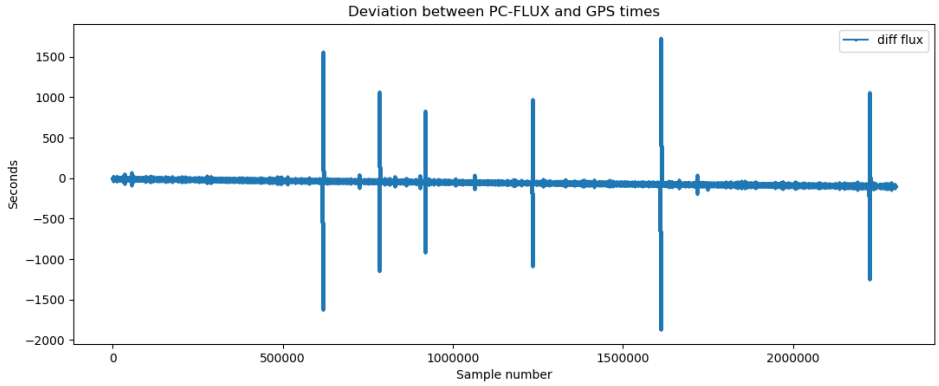

Figure 7. Time difference between the PC-FLUX clock and the GPS time

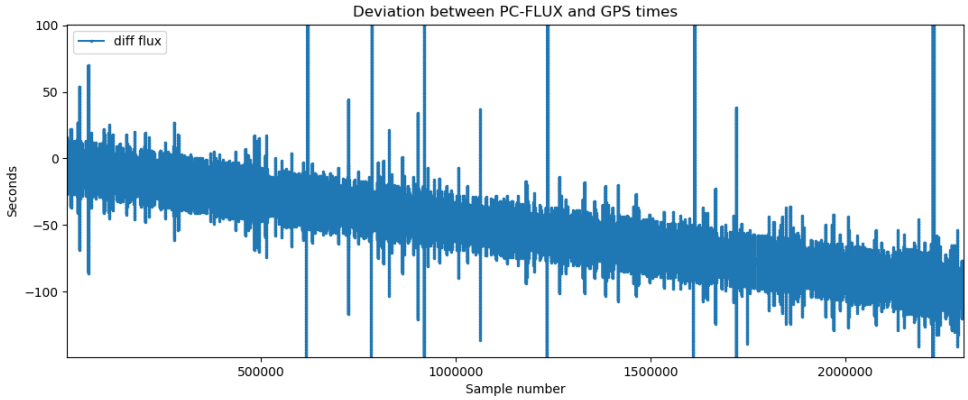

Figure 8. Zoom in Figure 7 data

After data cleaning, *i.e.* after deletion of the lines that were received twice and of the lines for which the time was not recorded, which happened several times during the campaign, we obtain a more explicit plot (Figure 9).

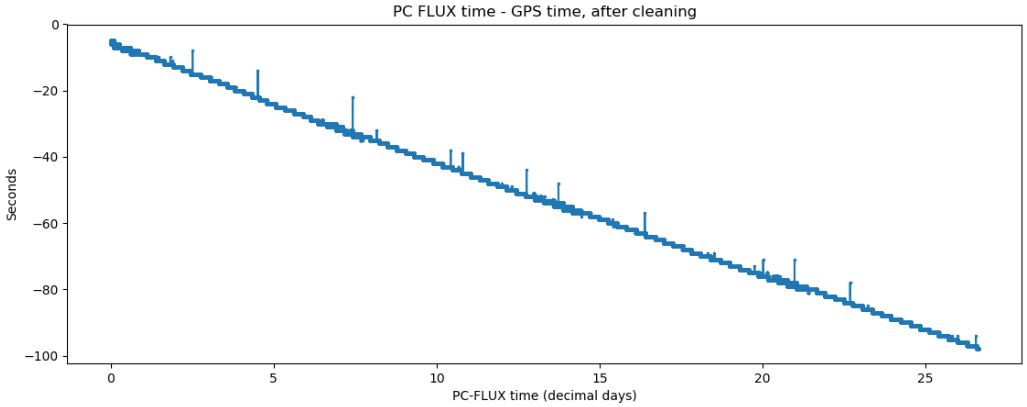

Figure 9. PC-FLUX time drift, after data cleaning, over the whole campaign

For the data processing, we tested two options: (1) interpolating all data on GPS times when possible and (2) using the PC-FLUX time as a reference time, despite its gradual drift. The second option gave better results and was kept. With this choice, rapid data such as Licor data have a time difference with respect to Gill data, which has consequences on latent heat flux values estimated with the Eddy Covariance method (EC method hereafter, section 3).

The BATOS data (routine ship data) also have a time shift with respect to the PC-FLUX time. However, it is less problematic for the 1 100 second time averages used throughout the manuscript than for rapid data such as Licor, as mentioned above.

As a summary, the PC-FLUX time is used for CR1000, Gill-BEI, and refractometer data, the PC-Licor time is used for Licor data, and the ship time (GPS) is used for BATOS data.

1.3 First overview of meteorological data

1.3.1 Comparison between WXT, CNR4, and BATOS data

Pressure, temperature, the radiation solar flux, and humidity were measured by several meteorological instruments (WXT, CNR4, refractometer, Licor, and BATOS data). Prior to any synchronization effort, it is already possible to compare them qualitatively, which gives an indication on the time extent over which each instrument was operational.

The WXT, CNR4 and BATOS data are available on a common range from 22 January at 3h00 UTC to 17 February at 18h00 UTC. Some sensors stopped functioning correctly after 15 days of experiment.

Pressure data from the WXT and the BATOS stations have a good visual fit to each other (Figure 10). However, the refractometer pressure data started to drift at day 17. Gaps are present in Licor pressure data (data in orange), which reveals conditions for which the R/V was not facing wind (see hereafter).

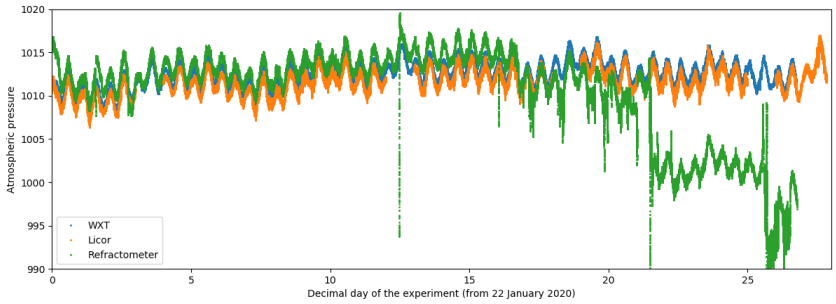

Figure 10. Atmospheric pressure measured by three sensors

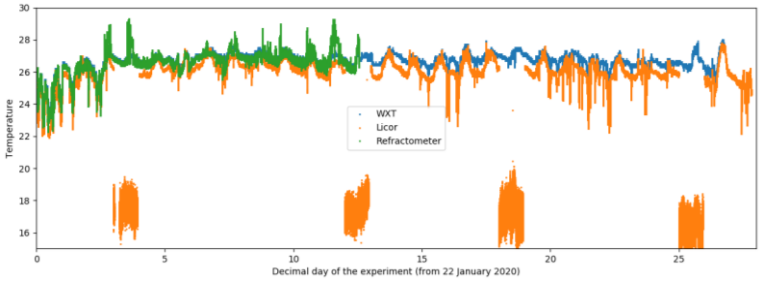

Figure 11. Air temperature measured by three sensors

The plot for air temperature further confirms that gaps in LICOR data correspond to rear wind conditions (not filtered out at this stage of the processing), as shown in Figure 11. LICOR temperatures have an overall negative bias with respect to WXT data, and have are more noisy. The refractometer temperature sensor stopped functioning from day 13.

Humidity data from the LICOR and the WXT have a good fit to each other (Figure 12).

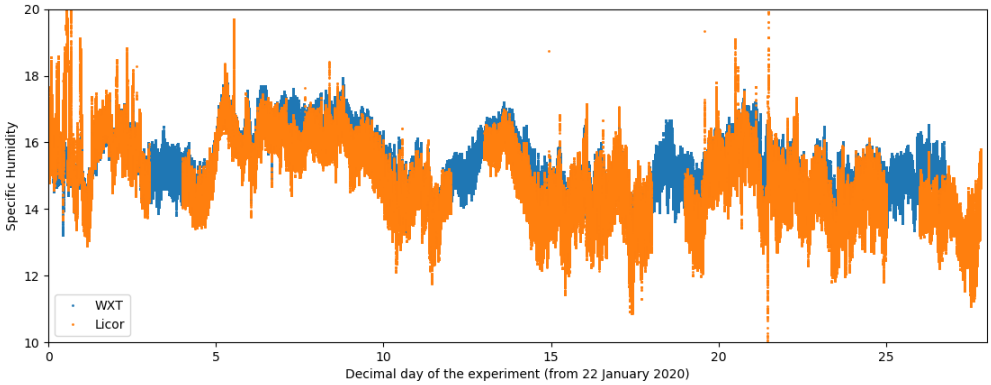

Figure 12. Air specific humidity measured by three sensors

The solar downward flux is measured by the BATOS system (on the top of the central mast of the ship, thus with no possible shadow effect, unlike with WXT data that are measured on the meteorological mast at the bow of the ship). A first comparison between BATOS and WXT data reveals that BATOS data have a threshold value at ~1040 W/m2, which does not happen with WXT data (Figure 13).

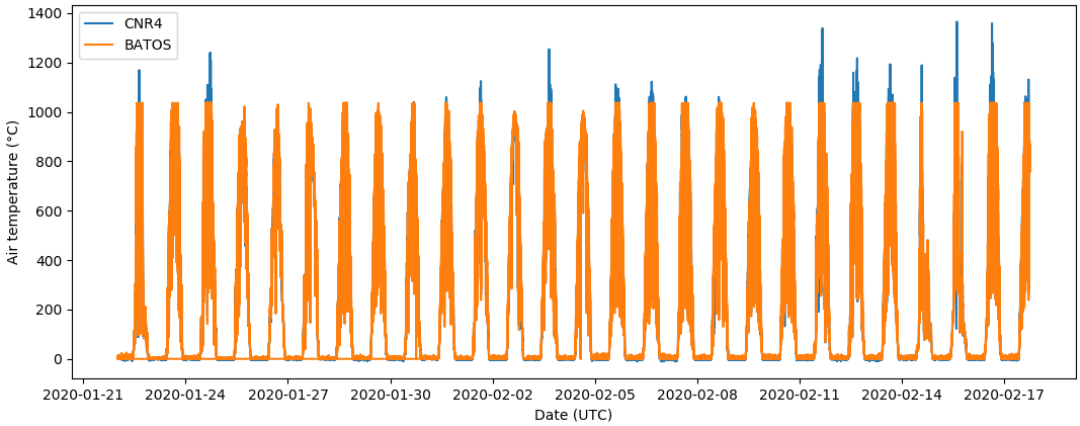

Figure 13. Incident solar flux measured by the BATOS system and by the CNR4 instrument

1.3.2 Known issues with the WXT sensors

The resolution of air temperature is 0.1°C and the resolution in atmospheric pressure is 0.1 hPa, which results in tabulated data (Figures 14, 15).

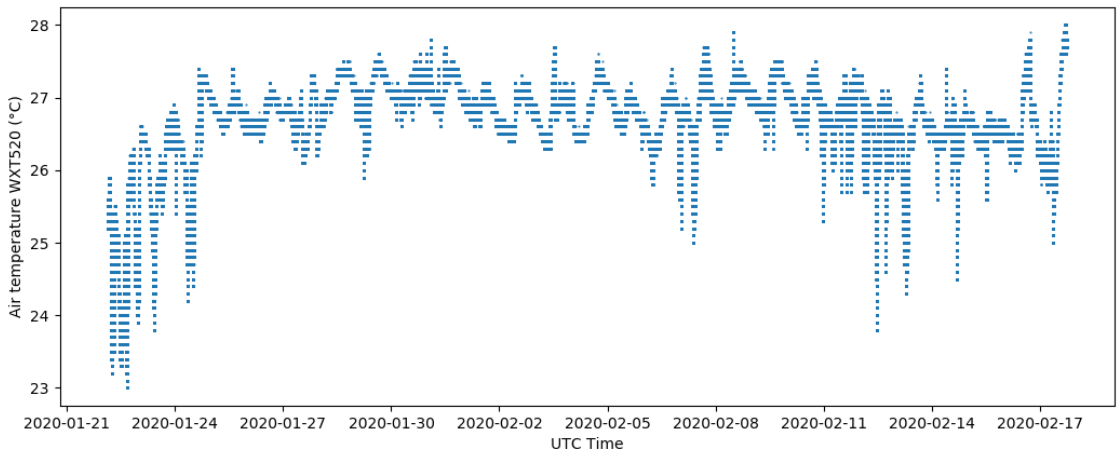

Figure 14. Tabulation effect in WXT air temperature data

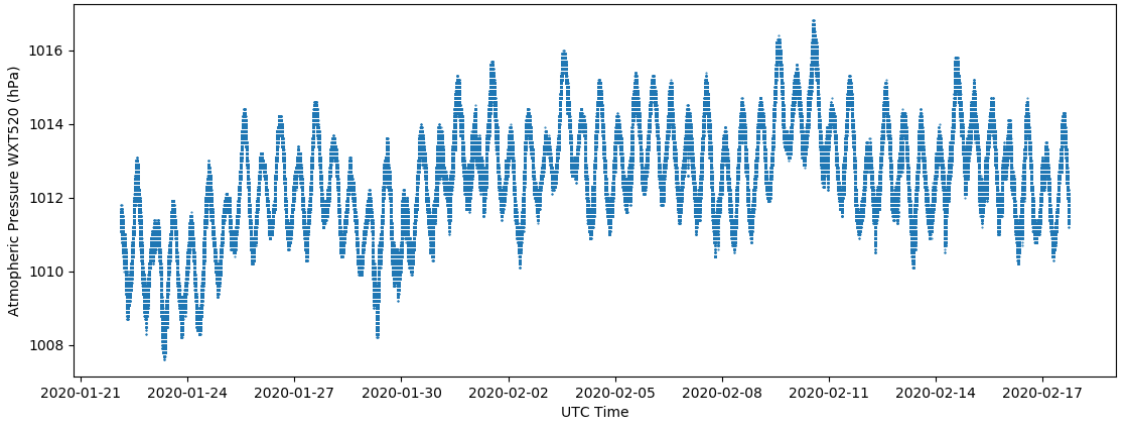

Figure 15. Tabulation effect in WXT atmospheric pressure data

Due to the location of the CNR4 at the top of the bow mast, the down-looking solar and infrared sensors are in direct view of the front deck, the temperature of which may be overestimated under the effect of solar warming, which may affect the upward flux data (Figures 16, 17). As a consequence, upward CNR4 fluxes are not used in the rest of the study. An albedo of 0.02 is used for deducing the upward solar flux from its incoming counterpart. For the upward infrared flux, the Sea Surface Temperature (SST) is used, with an emissivity of 0.98.

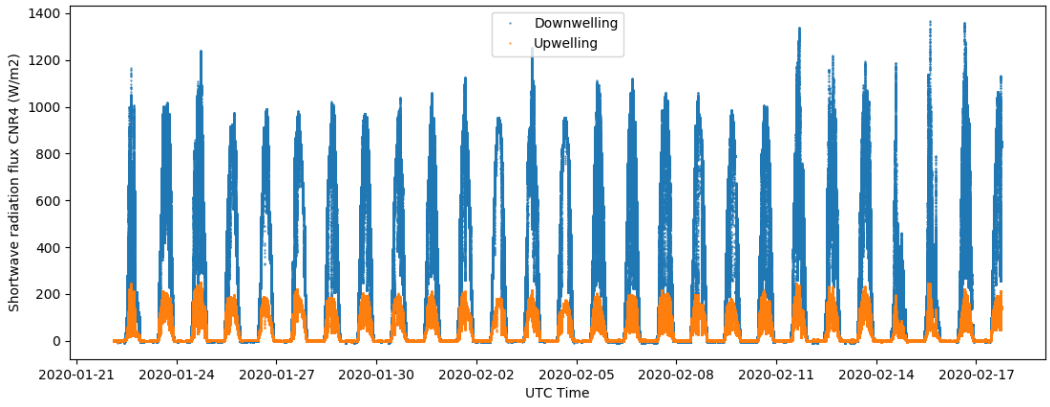

Figure 16. Solar flux from CNR4 data

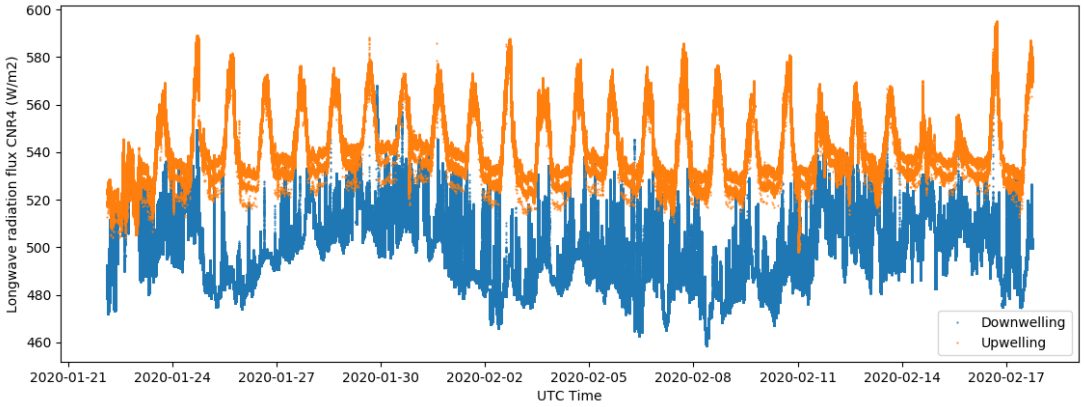

Figure 17. Infrared fluxes from CNR4 data

1.4 Application of quality criteria

The data processing for flux estimation fully corresponds to the existing Albatros flux processing code developed for the OCARINA platform, which is available at:

(https://gitlab.osupytheas.fr/bourras.d/albatros_public_distrib/-/blob/master/README.md).

During the processing, each day of the experiment is divided in time intervals of 1 100 seconds, which is the integral time of turbulence. For example, it means that the air temperature data output from the flux algorithm corresponds to averages over 1 100 second-intervals. Data are selected according to the following criteria, which are intended to provide a basic non supervised cleaning of the data:

- **max_anguh**, Float, [40.]. Maximum azimuth angle tolerated, in degrees (the wind angle with respect to the bow of the ship, to avoid flow distortion that occurs when the wind comes from the side or from the rear of the R/V)
- **minmax_angle**, Float, [50.]. Maximum variation of the azimuth angle tolerated during the time interval, in degrees (to make sure that the R/V is not turning)
- **std_angle**, Float, [10.]. Maximum tolerated for the standard deviation of the azimuth angle during the time interval, in degrees
- **minmax_fit_angle**, [30.]. Maximum tolerated variation for the linear fit to the azimuth angle values along the time interval, in degrees
- **vbf_minmax**, Float, [2.]. Maximum tolerated variation of the 3rd degree fit to ship speed, in m/s (to make sure that the ship is not accelerating or decelerating)
- **vbf_moy_min**, Float, [0.]. Minimum ship speed in m/s
- **eps_refracto**, Float, [1.00000000e-06]. Convergence condition for refractometer humidity calculation
- **ibo_max_refracto**, Int, [20.]. maximum number of iterations for refractometer humidity calculation
- **min_ta, Float**, [2.]. Minimum acceptable air temperature (Celsius)
- **min_sst, Float**, [5.]. Minimum acceptable sea surface temperature (Celsius)
- **min_psurf**, Float, [900.]. Minimum acceptable atmospheric pressure (hPa)
- **min_hr**, Float, [20.]. Minimum acceptable relative humidity (0-100)
- **max_diff_time**, Float, [2.]. Maximum acceptable time gap between two successive samples of the time interval in process (seconds)

- **percent_data**, Float, [100.]. Minimum percentage of valid data in the processed time interval required to proceed with the flux calculation (0-100)
- **lmo**, Float, [9999.]. First ID algorithm convergence condition. Maximum value of the Monin-Obukhov length tolerated during ID calculation
- **eps_zlidm**, Float, [1e-5]. Second ID algorithm convergence condition. Convergence is obtained when the absolute value of the difference between two successive evaluations of the Monin-Obukhov ratio is smaller than this value
- **ibo_max**, Float, [50]. Third ID algorithm convergence condition. Maximum number of iterations tolerated for convergence

Out of the 27 days of the experiment, the application of the above criteria reduce the number of data to 140 useful hours (5.84 days), which represents a rate of return of 22 %. Please note the maps does not show the numerous CTD stations when the R/V was standing (Figure 18).

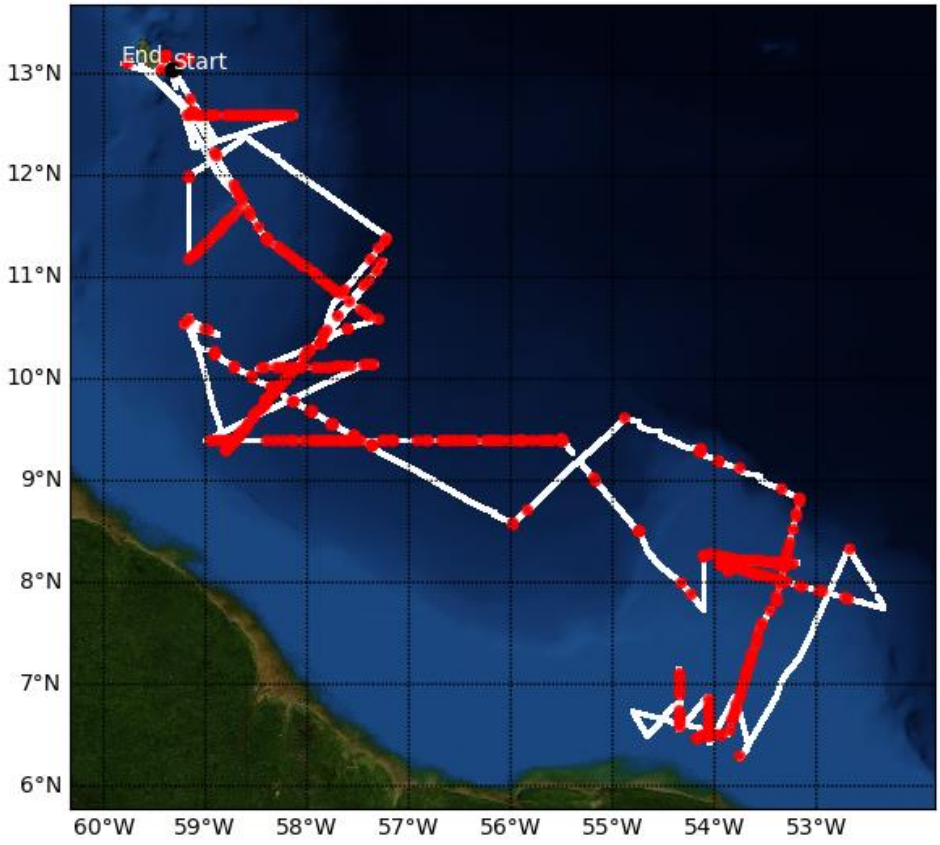

Figure 18. Map of the EUREC4A Atalante cruise (white dots). The data retained for flux calculation are plotted in red.

2. Meteorological data

2.1 Data from slow instruments (WXT, CNR4 et BATOS)

The comparisons between WXT and BATOS data are good in terms of correlation coefficients. However, biases are present (Figure 19).

For atmospheric pressure, the bias is not significant (0.05 hPa).

For air temperature, the BATOS data are underestimated by -0.1°C which is small, and may be true because BATOS data are taken about ten meters above WXT data, and the boundary layer is convective most of the time, which means that temperature decreases with altitude.

The BATOS relative humidity is larger by 4% than the WXT humidity, which translates into a large bias of 0.8 g/kg in terms of specific humidity.

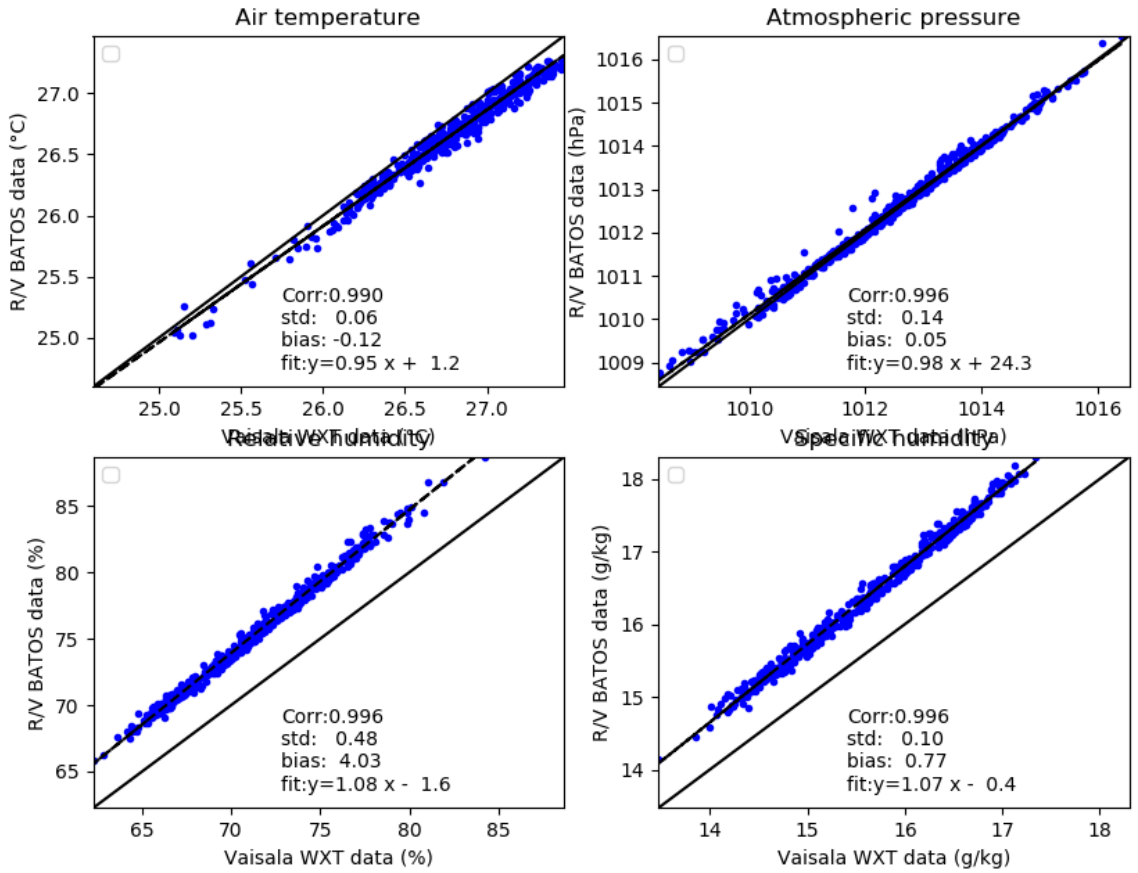

Figure 19. Comparison between WXT and BATOS data for 1 100-second averages

The comparison between WXT and BATOS wind data is good. However, a group of points are overestimated by the BATOS data. The overall bias is positive (+0.6 m/s for BATOS data, Figure 20), which is compatible with the idea that wind increases with altitude.

The wind direction data from the BATOS and the WXT data are in good agreement. Please note that at large wind angles, a distortion effect is noticeable. The effect is not symmetrical and it depends on the side from which the wind blows on the sensors.

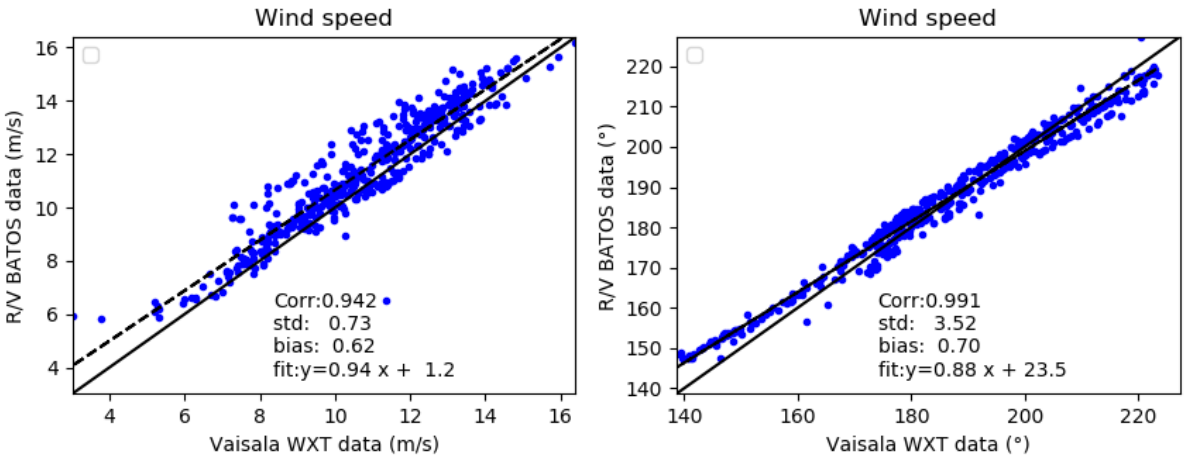

Figure 20. Comparison between WXT and BATOS data for 1 100-second averages

The overestimated outlier points in Figure 20 (left) are not elucidated. We checked that they did not occur for a single day, but that they occurred episodically all along the experiment (not shown).

The downward solar flux data from the BATOS are slightly overestimated (~5 W/m2) compared to the CNR4 data, which may reveal some shadow effects on the CNR4 sensors (Figure 21). The threshold at 1 040 W/m2 previously noted translates here into a slight underestimation of the largest BATOS data. The standard deviation is significant (20 W/m2) and is considerably smaller at small flux values (< 200 W/m2).

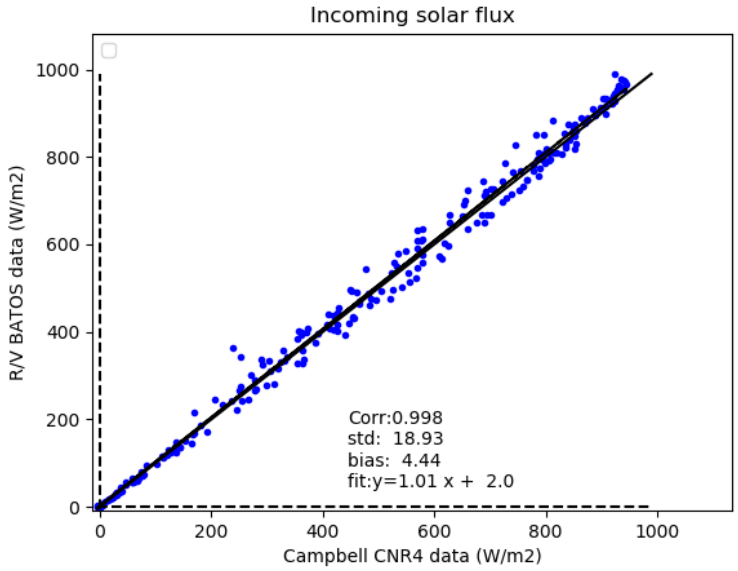

Figure 21. Comparisons for the incoming solar flux

2.2 Comparison to fast sampling rate instruments

2.2.1 Sonic anemometer data

2.2.1.1 Wind

The « apparent » wind vector is measured by the Gill and the WXT instruments, which are not at the same altitude: the WXT is ~1 m below the Gill instrument. The Gill is one meter ahead with respect to the WXT, which is closer to potential aerodynamic obstacles such as the mast (Figure 3). The observed module of the wind vector is smaller by -0.4 m/s according to Gill data than to WXT data (Figure 22).

The comparison also indicates a slope of linear fit that is significantly far from unity (0.86), which means that strong winds are more overestimated by the WXT. We suspect here that the WXT is the object of a local flow distortion (Venturi) effect. As already observed with respect to the BATOS data (Figure 20), a group of points are strongly underestimated by the WXT, which is attributed to an effect of distortion. It is not fully explained by the difference in wind direction from the Gill and the WXT (Figure 22, right), although the large angles have more bias than the small angles. If these outlier points are not accounted for, the bias between Gill and WXT data is -0.76 m/s, which is large.

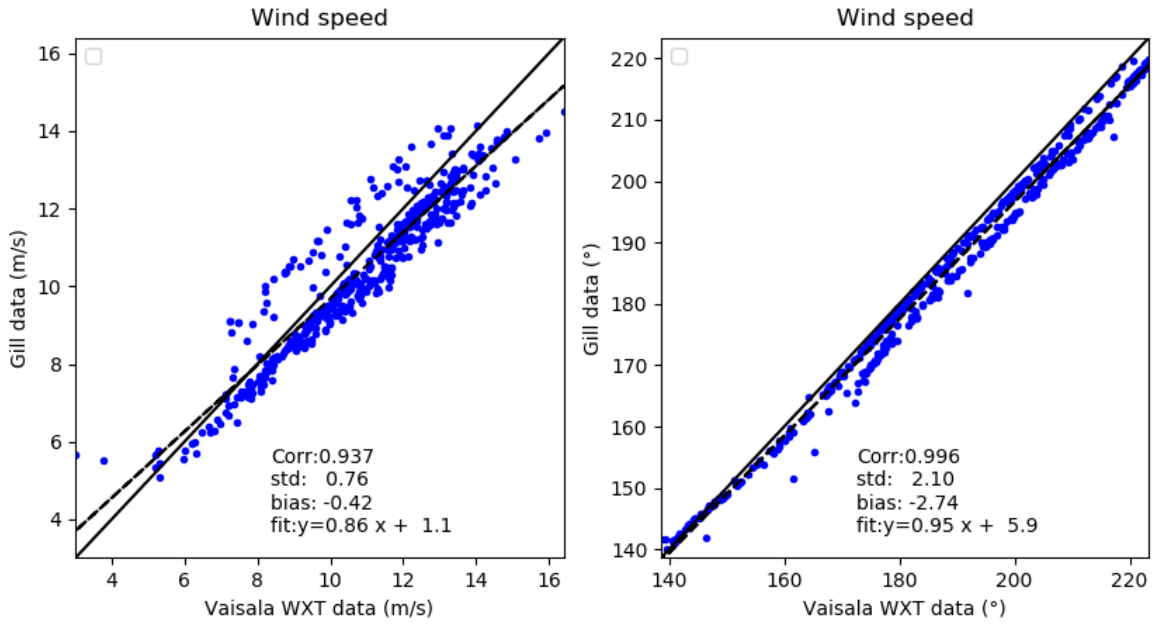

Figure 22. Comparisons between Gill and WXT wind speed (left) and apparent direction (right)

The comparison between Gill and BATOS wind data brings a new point of view as the group of outlier points no longer appears. As a result, the outliers occur only with WXT data. The standard deviation of the difference between Gill and BATOS data is good, 0.4 m/s, but the slope of linear fit to data is still smaller than unity (0.89).

The bias of Gill minus WXT wind speeds is 1 m/s, which is large. A quick calculation of wind difference at the two altitudes of the Gill and the WXT results in an expected wind difference of u*/kappa ln(20/15)= 0.2 m/s, for a height difference of 5 m. Therefore, the large 1 m/s bias is rather explained by distortion effects that differ according to the location of the sensors than by a height difference. The bias both corresponds to suspected effects of (1) slow-down of the wind at the location of Gill

data, and (2) artificial increase of the wind at the level of the BATOS sensor (Venturi effect). Simulations were already performed around the body of the Atalante in Bourras et al. (2009). The simulations revealed that wind speed was reduced, but only by -0.2 m/s at the level of the Gill instrument at 0° wind angle (Figure 5a in Bourras et al., 2009). The simulations also predicted the overestimation of the direction at the large wind angles. Unfortunately, the simulations were not analyzed at the location of the BATOS wind sensor.

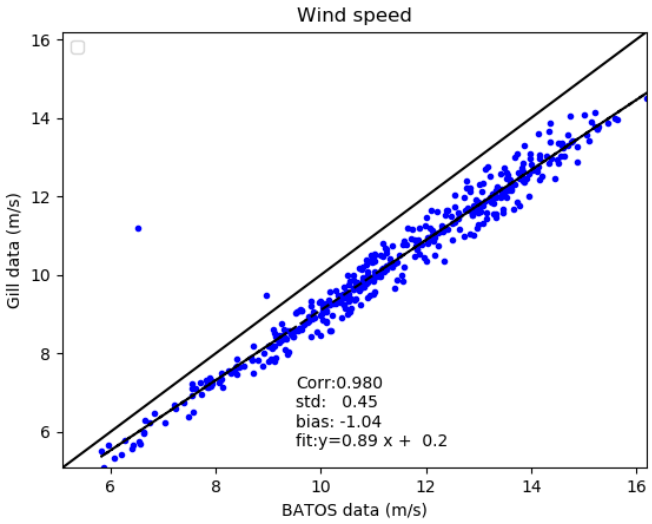

Figure 23. Comparisons between Gill and BATOS wind speed

In doubt, hereafter, Gill data are considered as reference data and a negative bias of -0.2 m/s has to be accounted for giving error bars.

2.2.1.2 Sonic temperature

The sonic air temperature is output from Gill data. It is possible to convert WXT air temperature and humidity to equivalent sonic temperature data. The comparison between Gill and WXT sonic temperatures reveals a large bias (Figure 24), which is a known issue with sonic data. More surprising is the poor correlation coefficient (0.56), which suggests that Gill data are not accurate for long term (1 100 sec) averages.

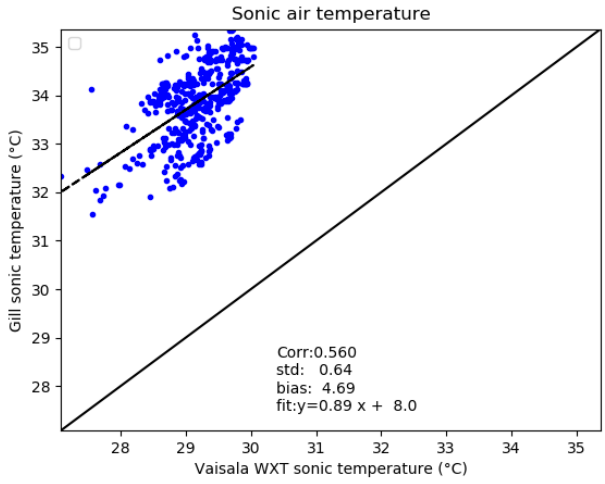

Figure 24. Comparisons between Gill and WXT sonic air temperature

Please note that other comparisons were done, with Gill data converted to true air temperature with refractometer or Licor data (not shown), and that the results were qualitatively the same as in Figure 24.

2.2.2 Comparison to Licor data

2.2.2.1 Ancillary sensors

The Licor has its own meteorological sensors for air temperature and pressure. Many data from these sensors have unrealistic values, thus they were avoided for the following comparisons, with respect to WXT data (Figure 15). Please note that the Licor is placed one meter above the WXT station on the mast.

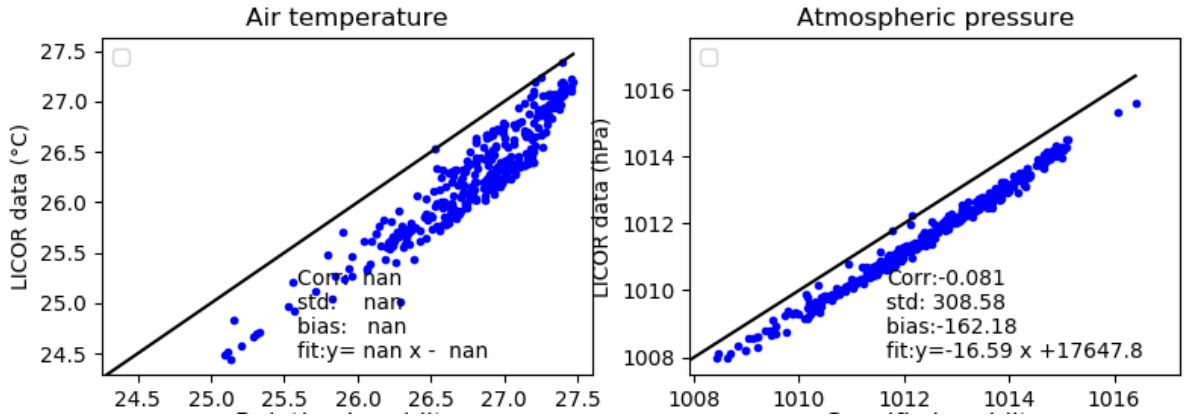

Figure 25. Comparisons between Licor (*y-axis*) and WXT data (*x-axis*)

Both the pressure and the temperature are significantly underestimated with respect to WXT data. As a result, we chose to use the averaged WXT data to calculate Licor humidity (given in g/m3), instead of using the Licor temperature and pressure sensors.

The results are presented in Figure 26. They show that a majority of points are underestimated with respect to WXT humidity data, by -2% and -0.5 g/kg, but that a large group of points is overestimated, as already noted for the wind speed.

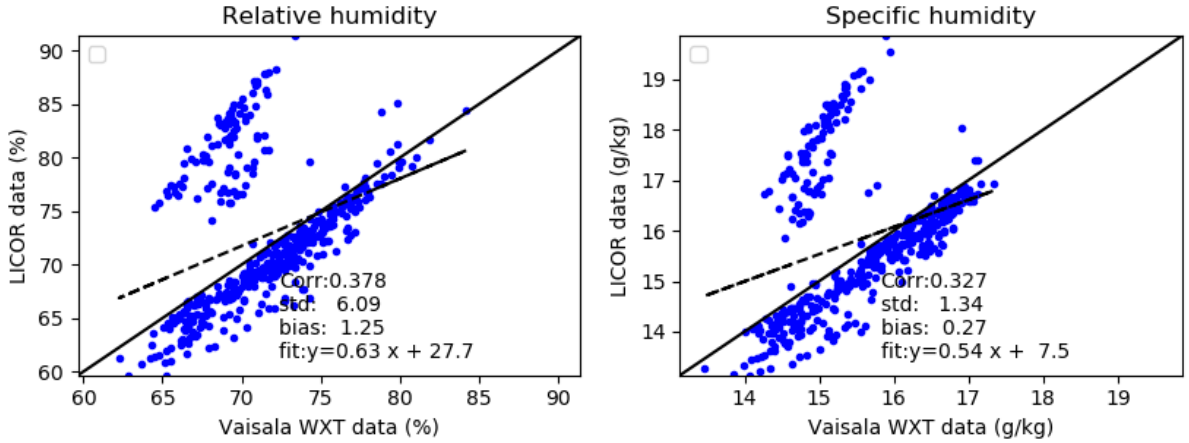

Figure 26. Comparisons between Licor (*y-axis*) and WXT data (*x-axis*)

In the previous section, we have shown that the WXT humidity was under-estimated by 4% with respect to the BATOS humidity, which again increases the uncertainty on humidity data. Indeed, the biases are as follows: humidity BATOS > humidity WXT > humidity LICOR.

As for the wind comparisons, we checked that the outliers were not concentrated at some days of the experiment (not shown), therefore they are challenging to avoid without seriously reducing the number of points.

2.2.2.2 Specific humidity from refractometer and from Licor data

In this section we compare the standard deviation of Licor and refractometer humidity. Power spectra of humidity from the two instruments will be compared in section 3.

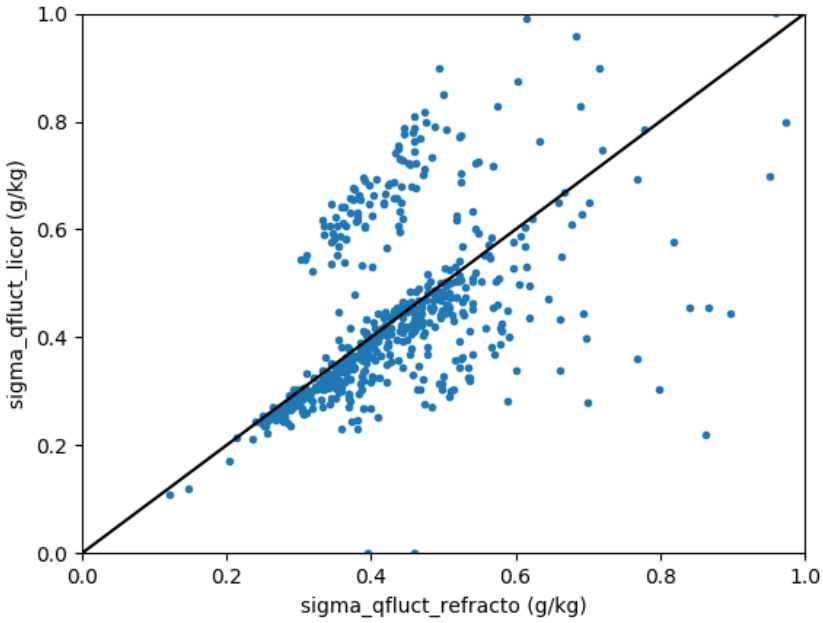

Figure 27. Comparisons between Licor (*y-axis*) and WXT data (*x-axis*)

Large values of the standard deviation of humidity are present but they are not shown in Figure 27, for readability. Apart for a group of outlier points, for which the standard deviation of Licor data are strongly overestimated with respect to refractometer data, the two types of data have a good fit to each other, with a slight overestimation for the refractometer, which is encouraging.

2.3 Wind distortion

The vertical wind angle is 5° at 0° azimuth angle for Gill wind data (Figure 27). For +/-40° azimuth angles, the vertical angle ranges from 3.5° to 7°, which translates into a vertical wind component from 0.4 to 1.4 m/s. This is consistent with the simulations in Bourras et al. (2009).

However, for EUREC4A data, we checked that accounting for the vertical wind angle in the calculation of the wind module resulted in an increase of the wind by 0.02 m/s to 0.1 m/s (not shown), which is negligible (see also section 3).

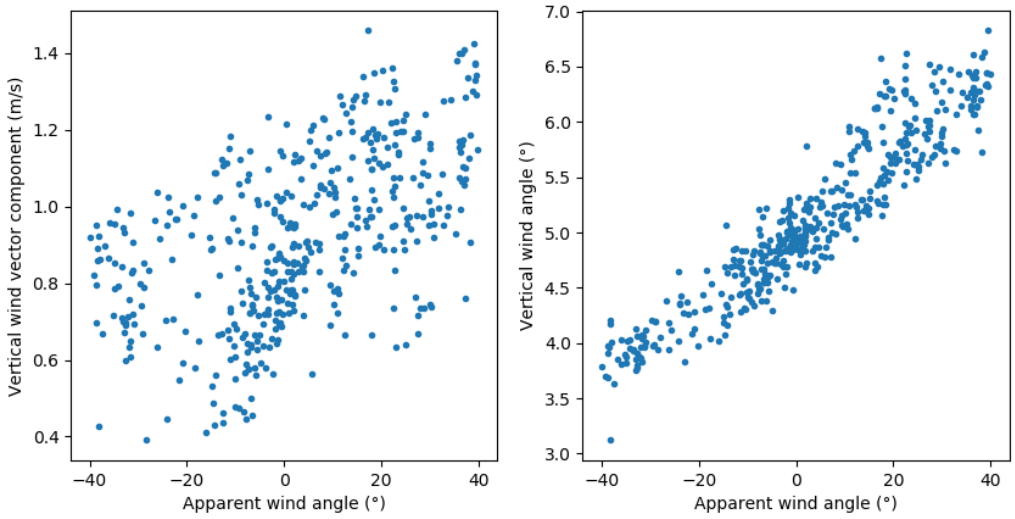

Figure 27. Vertical wind component (left) and vertical wind angle (right)

2.4 Comparison to OCARINA data

OCARINA is a drifting platform that has negligible flow distortion (Bourras et al., 2014 and 2019). It was deployed four times during the campaign (red dots in Figure 28).

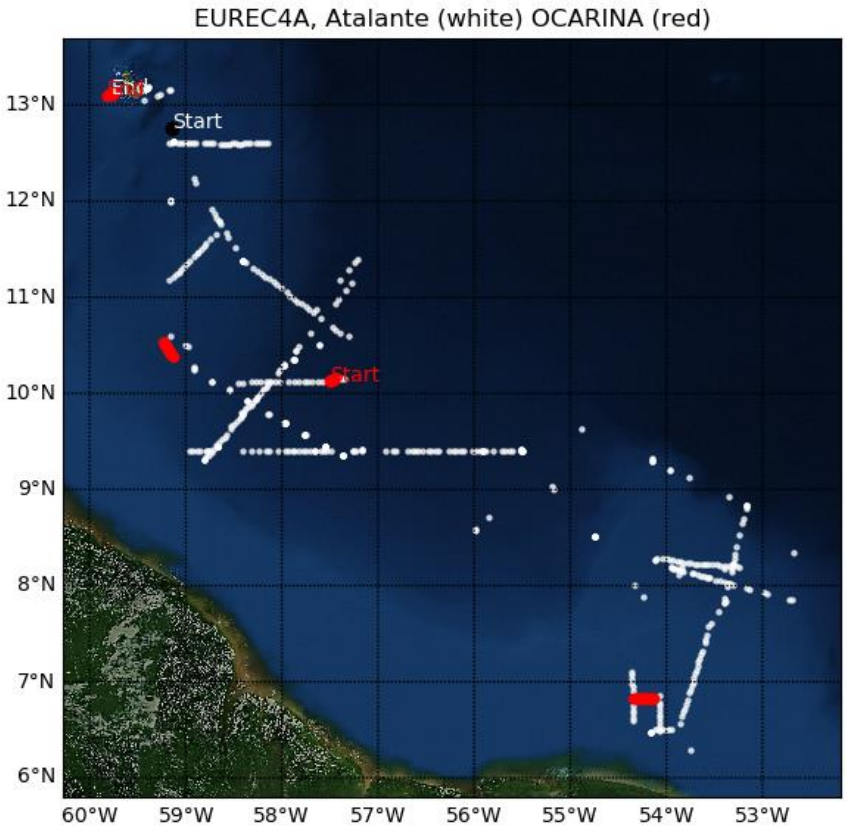

Figure 28. Locations of the OCARINA deployments (red dots) compared to the available Atalante flux mast data (white dots)

For comparing OCARINA data to Atalante data, we restricted the data choice to maximum time deviations of +/-1 hour. It results in only 21 points of comparison and to a maximum distance of 15 km between the two platforms (Figure 29).

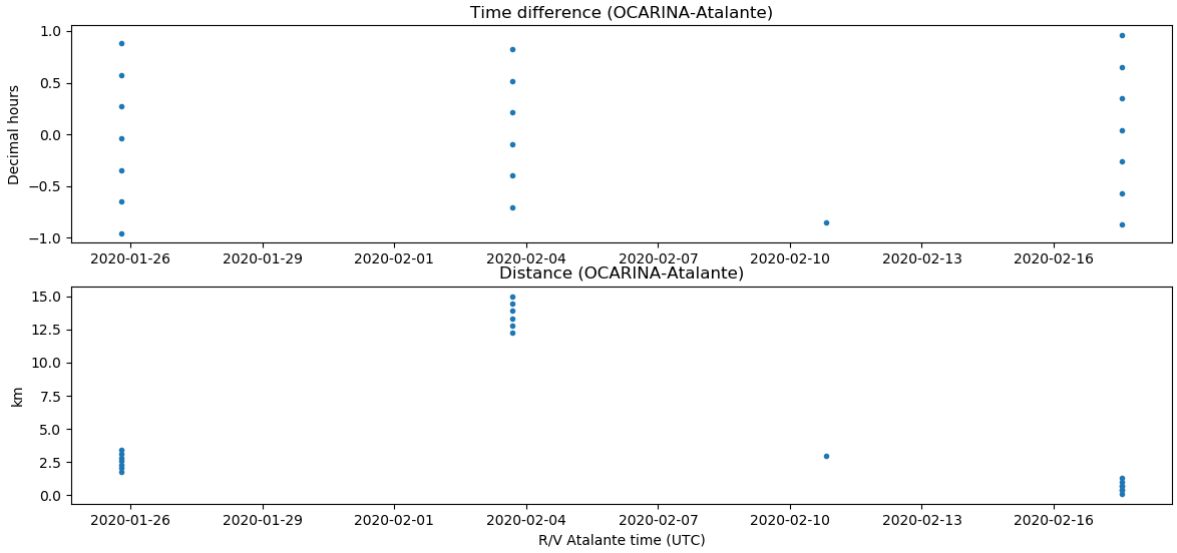

Figure 29. Data selected for comparison between OCARINA and Atalante data. The distance (lower panel) and the time diference (upper panel) are plotted as a function of time.

Given the small number of points of comparison, the comparisons presented hereafter are just an indication and not a reliable comparison, from a statistical point of view.

The first raw comparisons are made with data taken at different altitudes and depths (Figure 30). They show acceptable correlation coefficients, larger than 0.67. There is a noticeable positive bias of OCARINA specific humidity data compared to Atalante WXT data (+0.74 g/kg).

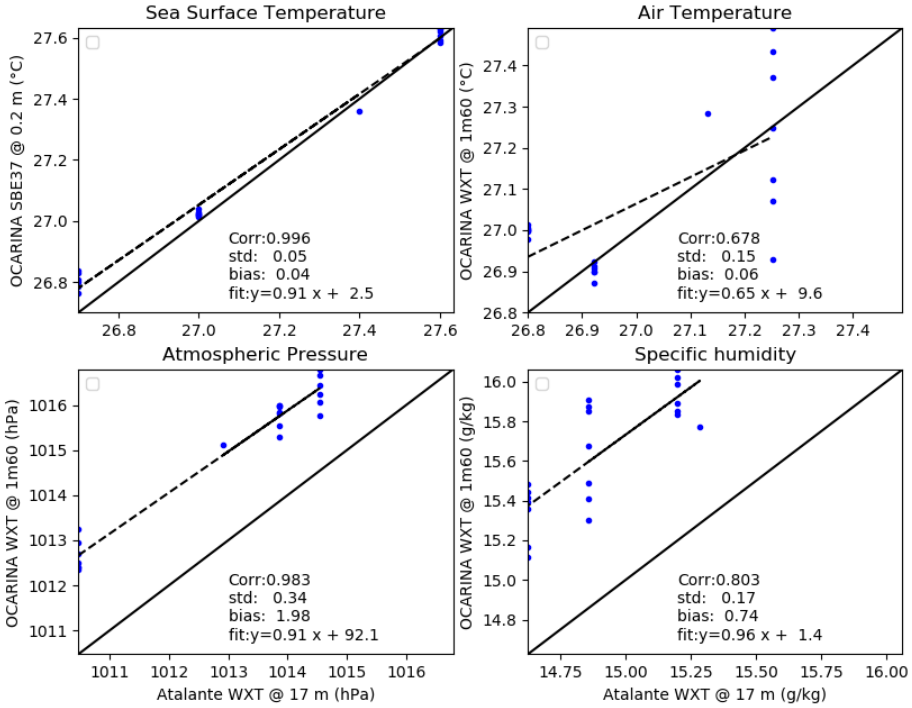

Figure 30. Comparison between meteorological data from OCARINA and Atalante at their respective heights of measurements

The comparison in terms of wind speed indicates that the Atalante wind speed (Gill data) is larger in average than the OCARINA wind speed, by +0.8 m/s (Figure 31). A positive bias was expected given the 15 m in height difference between the two sensors.

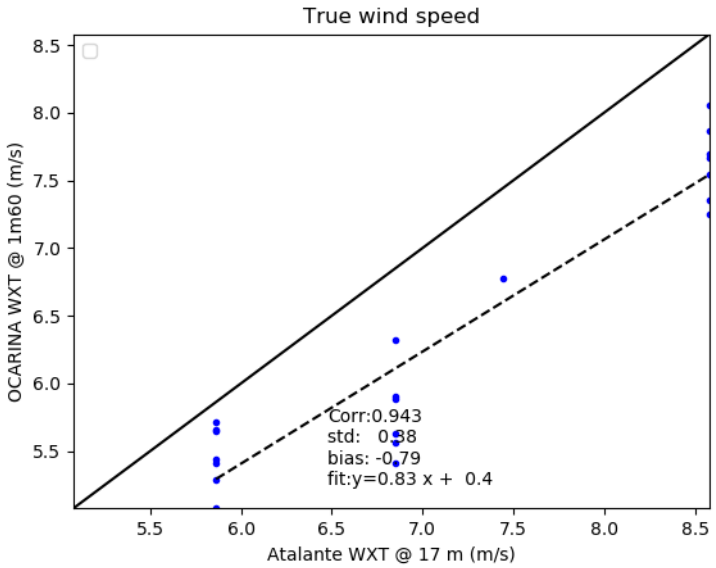

Figure 31. Wind speed comparison

The comparisons in terms of 10 m-neutral variables bring a further insight, although it is anticipating on section 4 results (application of the bulk COARE 3.0 algorithm), as shown in Figure 32.

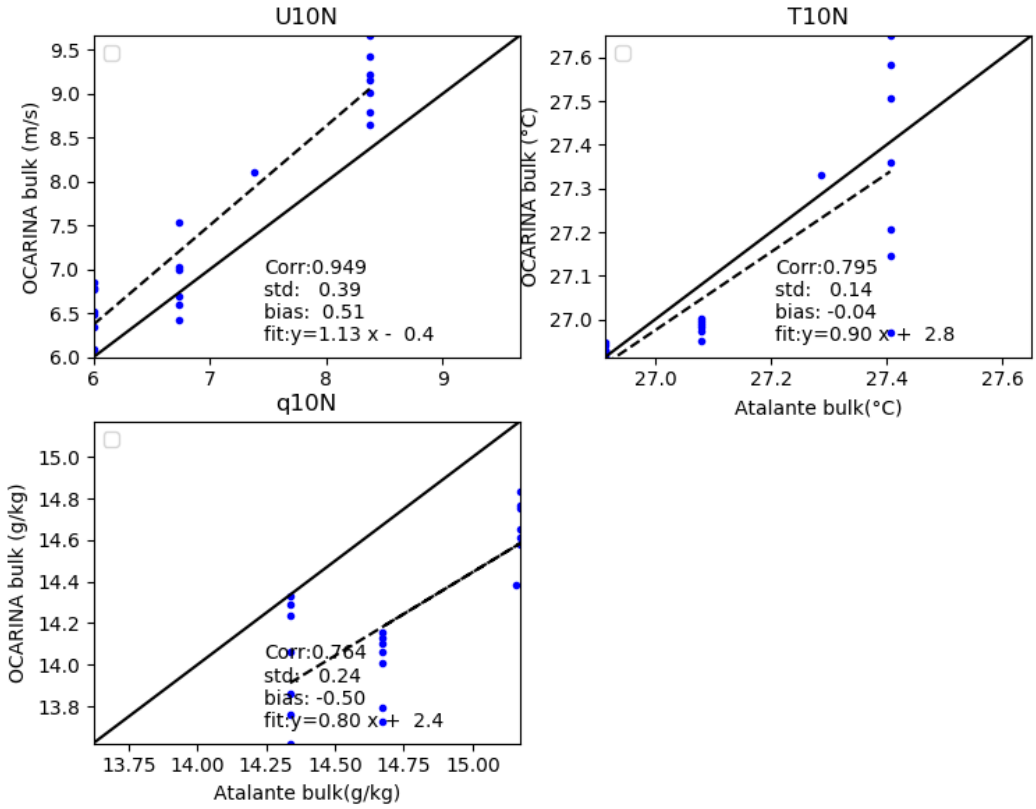

Figure 32. 10 m-neutral wind, temperature, and humidity comparison

OCARINA U10N are overestimated by 0.5 m/s with respect to Atalante U10N estimates (Figure 32), which may suggest that Atalante data are affected by flow distortion, which was expected according to the simulations (-0.2 m/s, section 2.2.1.1).

The comparisons for q10N (the neutral specific humidity at 10 m) shows a negative bias of 0.5 g/kg, which means that Atalante WXT data converted to 10 m neutral conditions are overestimated with respect to OCARINA data. Therefore, 10 m-neutral humidity WXT Atalante > 10 m-neutral humidity WXT OCARINA.

2.5 Conclusions

The observed bias are:

- Air temperature
  - WXT > BATOS (+0.12 °C)
  - WXT > LICOR (+0.4 °C)
  - T10N ATALANTE WXT > T10N OCARINA WXT (+0.04°C)
- Atmospheric pressure
  - WXT < BATOS (-0.05 hPa)
  - WXT > LICOR (+0.5 hPa)
  - ATALANTE WXT < OCARINA WXT (-2 hPa)
- Relative humidity
  - WXT < BATOS (-4.03%)
  - WXT > LICOR (+2%)
- Specific humidity
  - WXT < BATOS (-0.77 g/kg)
  - WXT > LICOR (+0.3 g/kg)
  - Q10N ATALANTE WXT > Q10N OCARINA WXT (+0.5 g/kg)
- Wind speed
  - WXT < BATOS (-0.62 m/s)
  - WXT > GILL (+0.42 m/s)
  - GILL < BATOS (-1.04 m/s)
  - U10N ATALANTE GILL < U10N OCARINA GILL (-0.51 m/s)
- Incoming solar radiation flux
  - CNR4 < BATOS (-4.44 W/m2)
- Sea surface temperature
  - SST ATALANTE < SST OCARINA (-0.04°C)

According to the WXT datasheet, the meteorological data have the following accuracy:

- Air pressure : +/-0.5 hPa
- Air temperature : +/-0.3°C
- Relative humidity: +/-3%
- Wind speed : +/-0.3 m/s (or 3%, whichever is the larger)

Overall, the comparisons presented above show that our data generally comply with the relatively low accuracy of the WXT sensors. However, we note that:

- Atalante Gill wind speed data are possibly underestimated by 0.3 m/s (flow slew down by distortion)
- The measurement of absolute specific humidity is problematic, because we observe biases from -0.8 to +0.5 g/kg

The above numbers give an order of magnitude of the measurement uncertainties. In doubt, in the following, we prefer not to apply any correction to the meteorological data.

3. Spectral analysis of turbulent data

3.1 Power spectra

The envelope of the power spectra for the daily longitudinal wind component (Gill HS-50 data) shows a clear inertial sub-range between 2 and 7 Hz (Figure 33).

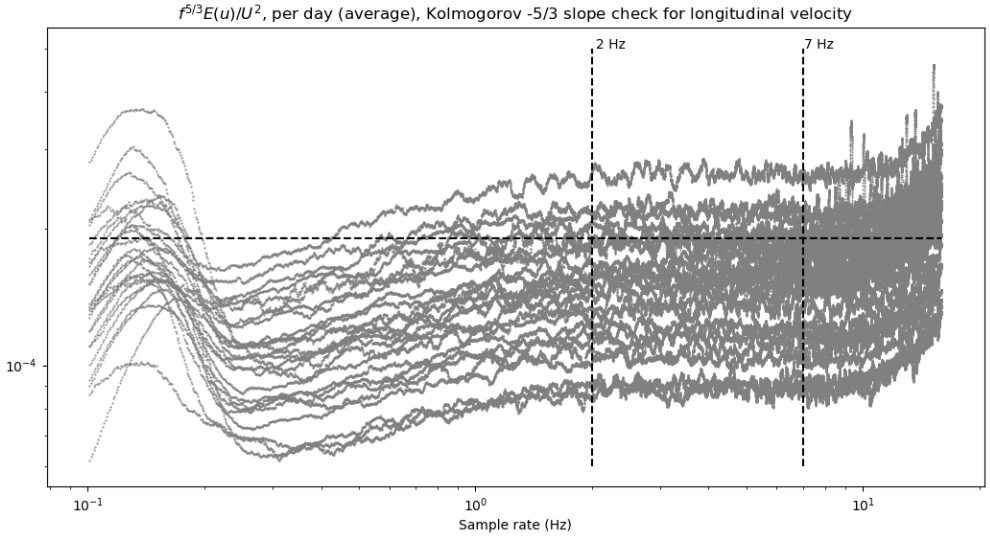

Figure 33. Normalized daily power spectra of the *u*-component of the wind vector, multiplied by $f^{5/3}$

The equivalent spectrum averaged over the entire data set further confirms that the [2 , 7] Hz range corresponds well to the sub-range (Figure 34). Hereafter, we even restrict this range to [3 , 6] Hz for safety.

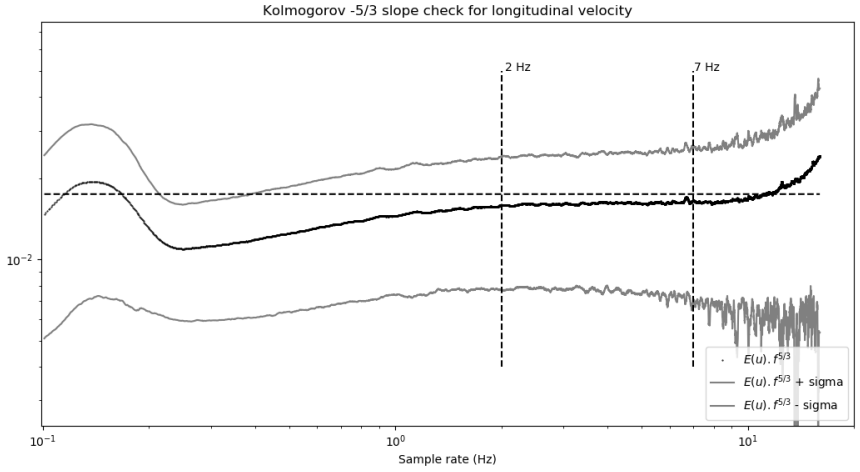

Figure 34. Averaged power spectra of the *u*-component of the wind vector, multiplied by $f^{5/3}$

The vertical isotropy Ew(f)/Eu(f) is quite well respected in the inertial sub-range (daily values close to the reference value of 4/3), as shown in Figure 35. However, the horizontal isotropy Ev(f)/Eu(f) is not well respected (Figure 36).

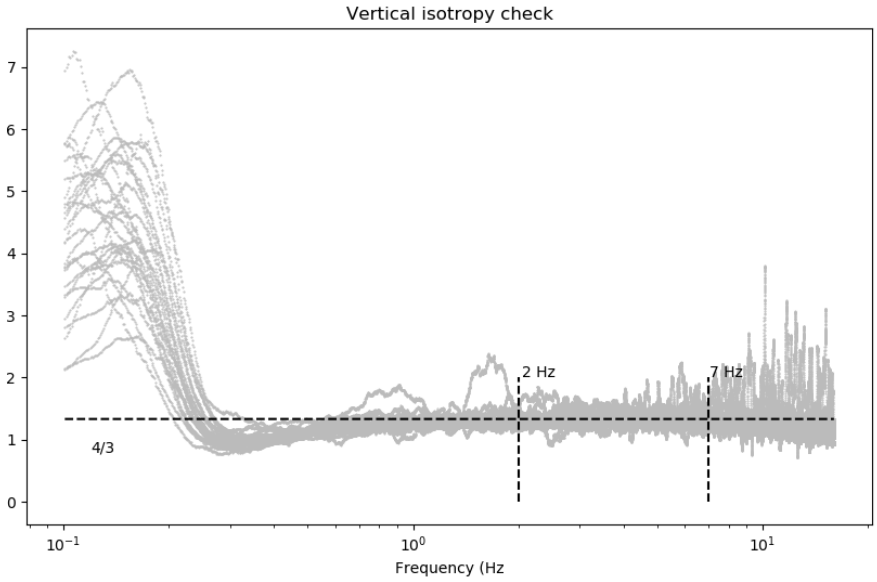

Figure 35. Departure of data from theoretical vertical isotropy (4/3)

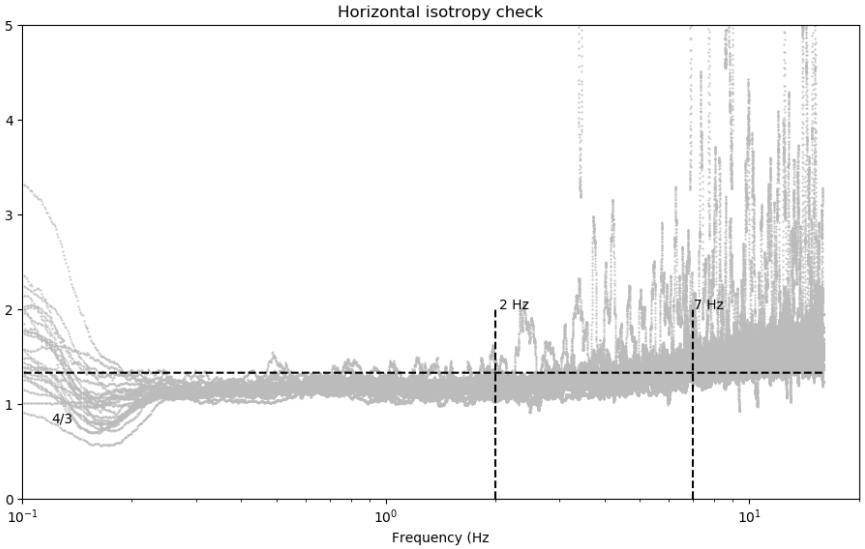

Figure 36. Departure of data from theoretical horizontal isotropy (4/3)

The power spectra for temperature do not generally follow a -5/3 log-log slope, which was also observed in earlier campaigns, even with OCARINA data that have small airflow distortion (Bourras et al., 2019). Hereafter, we use data in the range [1, 2] Hz. The envelope of curves is coherent, and there is only one day with outlier data (Figure 37).

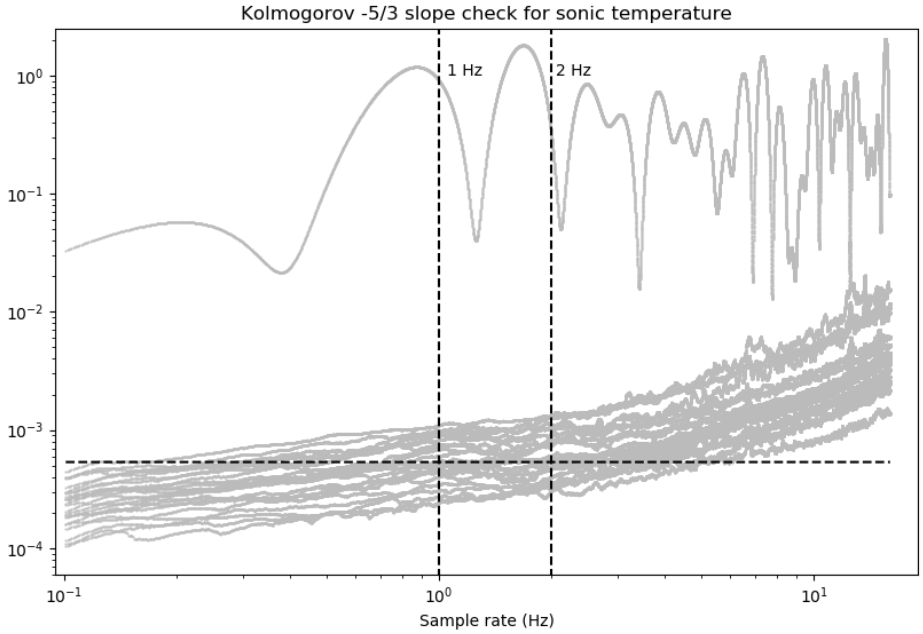

Figure 37. Normalized daily power spectra of the *sonic* temperature, multiplied by $f^{5/3}$

The sub-range in refractometer specific humidity data is well respected for certain days over a large [1 , 10] Hz range. Unfortunately, some of the daily spectra are increasing at frequencies larger than 2 Hz. In addition, there are two days with outlier data, for which the spectra are oscillating and have large values. As a compromise, we choose the [1 , 2] Hz interval as the sub-range in humidity.

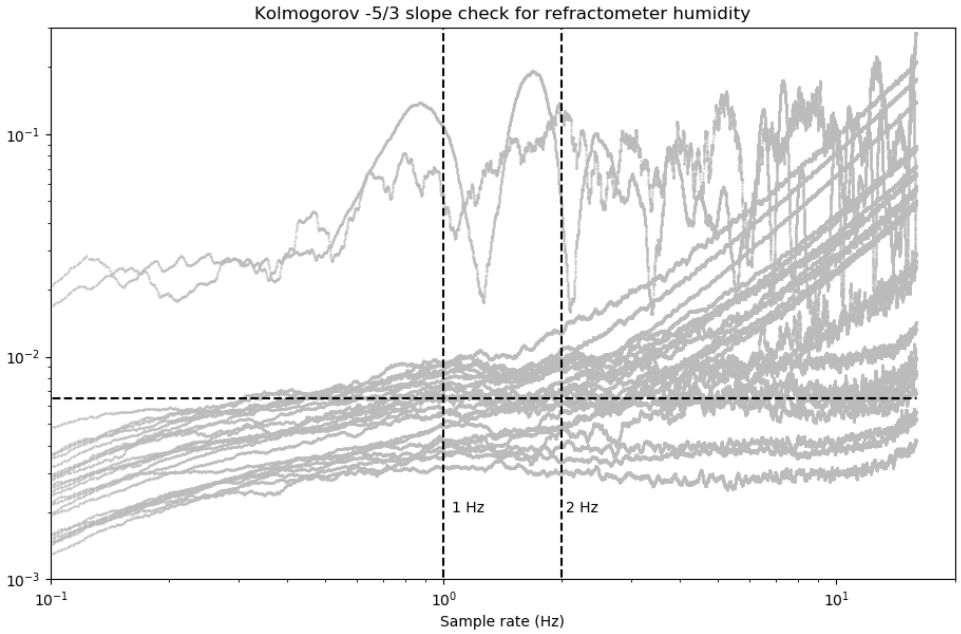

Figure 38. Normalized daily power spectra of the refractometer specific humidity, multiplied by $f^{5/3}$

The Licor spectra were more challenging to process as they included invalid data (Nan), which occurred for 2% of the data. After correction, *i.e.* the "Nan" values were replaced by arbitrary averaged values, we obtained the power spectra of Figure 39.

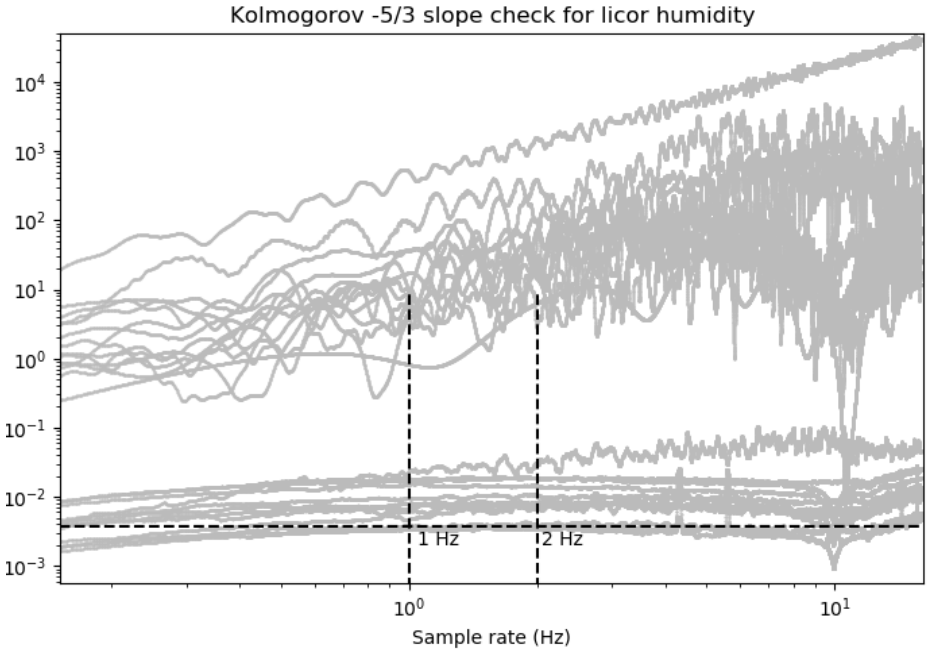

Figure 39. Normalized daily power spectra of the *LICOR specific humidity*, multiplied by $f^{5/3}$

According to Figure 39, the -5/3 slope is only respected for a small number of days (lower curves in Figure 39). The other daily spectra are all increasing with frequency, which is not elucidated at the stage of the processing.

3.2 Analysis of the co-spectra

3.2.1 Wind co-spectra

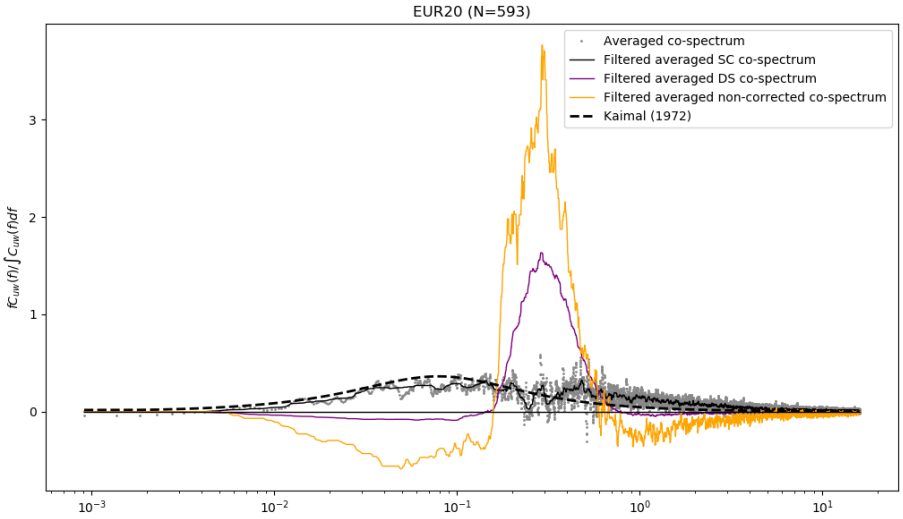

Figure 40. Averaged wind co-spectra, uncorrected (yellow), corrected with the DS method (purple), and correction with the SC method (black).

The wind co-spectra averaged over the whole data set, with no filtering of the *w*-component (in yellow) is very different from the reference spectrum of Kaimal et al. (1972). It has a zone of negative covariances in the turbulence production range, and it presents a large peak at fz/U=0.3, attributed here to the vertical motion of the ship (Figure 40). If the vertical wind component is corrected with a

basic subtraction of speed vertical speed (DS method, see Bourras et al., 2019), the large peak has a reduced intensity (curve in purple). The application of a spectral coherence (SC method, see Bourras et al., 2019) is the only method that efficiently removes the motion peak (black curve), and makes it coherent with the co-spectrum of Kaimal et al. (1972), which is better shown in Figure 41. This closer look at the co-spectrum reveals that it is more spread over frequencies than the reference Kaimal et al. (1972) co-spectrum. In addition, there is less energy in our data in the turbulence production frequency range (fz/U=0.1).

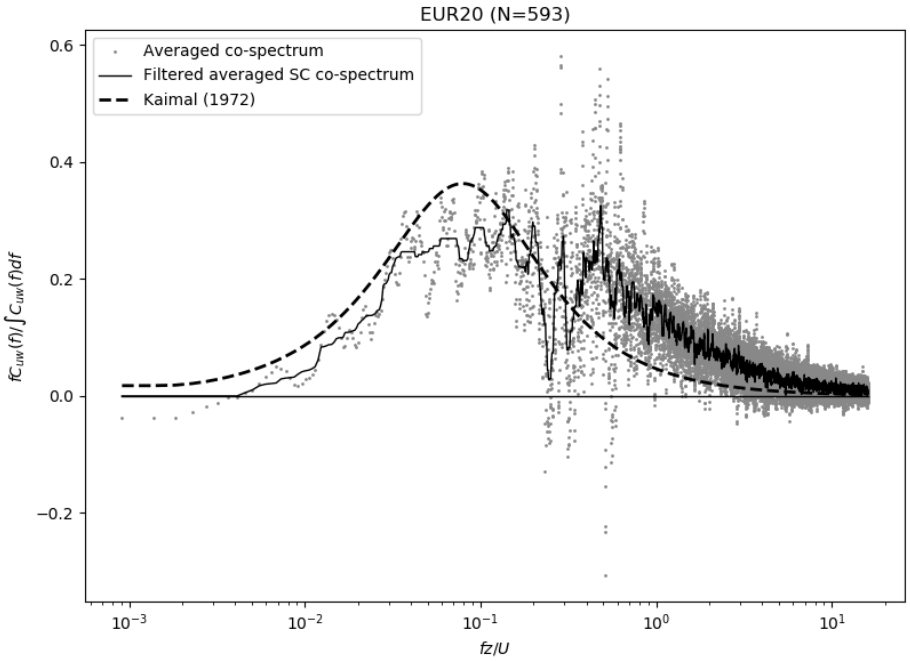

Figure 41. Averaged wind co-spectra with the SC correction of the vertical wind component

3.2.2 Humidity co-spectra

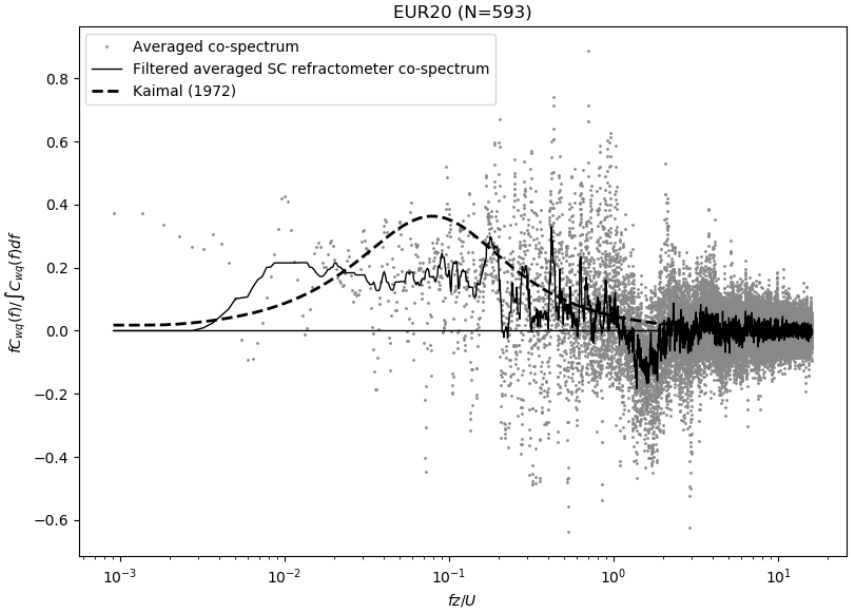

Figure 42. Averaged wind-refractometer humidity co-spectra, with the SC correction of the vertical wind component.

The averaged co-spectrum for refractometer specific humidity fluctuations has a large production zone, larger than the one of the reference (function H(z/L) in Kaimal et al., 1972) and it is shifted toward lower normalized frequencies. Again, the overall energy is smaller than in the reference spectrum (Figure 42).

The co-spectrum for the LICOR is noisy thus impossible to use (Figure 43).

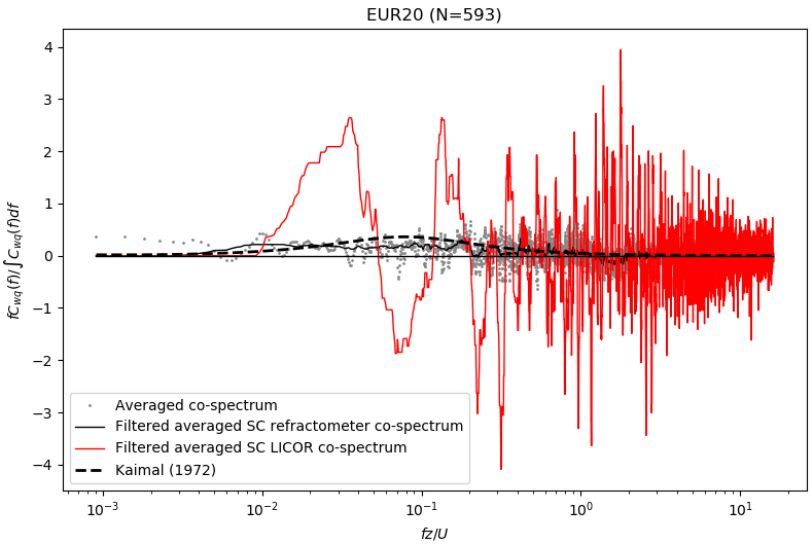

Figure 43. Averaged wind-LICOR humidity co-spectra, with the SC correction of the vertical wind component.

3.2.3 Temperature co-spectra

We present here the vertical wind versus sonic temperature averaged co-spectrum (Figure 44, black curve). Next, we plot the co-spectrum for air temperature, with humidity correction done with refractometer data (in red).

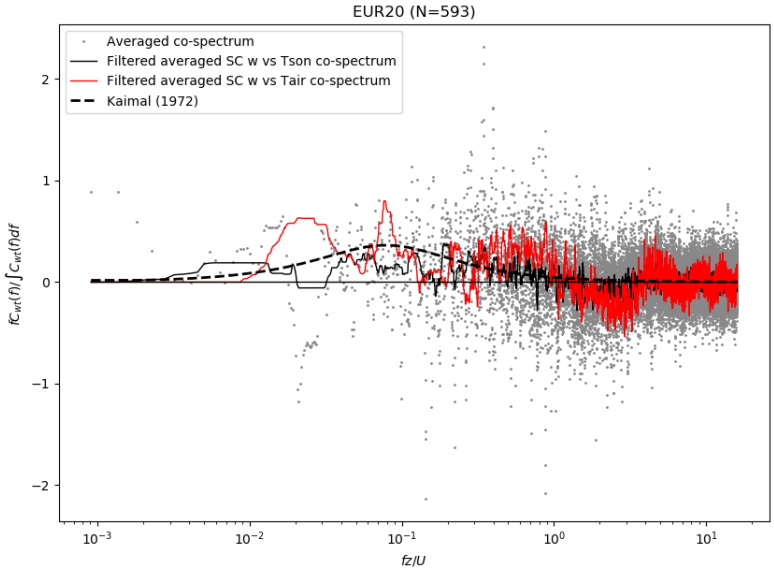

Figure 44. Vertical wind versus sonic (black) and true air temperature (red) averaged co-spectra, with the SC correction of the vertical wind component.

The temperature co-spectra are very noisy and do not even have a bell-like shape like in Kaimal et al. (1972).

3.3 Conclusions

In the wind power spectra, the inertial sub-range is well identified at [3.6] Hz. The vertical isotropy is well respected, as opposed to the horizontal isotropy of turbulence. Overall, this analysis suggests a good potential of the EUREC4A data for calculating the momentum flux with the inertial-dissipation (ID) method, largely based on the spectral properties of the turbulence in the inertial sub-range.

The temperature spectra do not really follow a -5/3 log-log slope, which has already observed in a number of earlier campaigns. In the [1 ; 2] Hz range, the -5/3 slope is reasonably respected, a choice that has already been made for earlier experiments.

Many of the daily humidity spectra do not follow the -5/3 log-log slope, which is unexplained at this stage. In this respect, the refractometer data behave better than the LICOR data. The [1 ;2] Hz sub-range was finally selected as a compromise, but the estimation of the latent heat fluxes with the ID method promises to be challenging.

The wind co-spectra clearly show that a correction of the vertical wind component is required, and that the SC correction method performs better than the DS correction method. Unfortunately, with the SC correction applied, the obtained co-spectra are generally underestimated with respect to the reference co-spectrum of Kaimal et al. (1972), which implies that the calculation of the momentum flux with the EC method will be underestimated.

The humidity co-spectra computed with LICOR data are too noisy to be used. For refractometer data, the averaged co-spectrum presents a bell shape, like in Kaimal et al. (1972). Unfortunately, the total energy of the co-spectrum is smaller than in the reference co-spectrum, which again suggests that the EC latent heat fluxes will be underestimated.

Last, the temperature co-spectra are very noisy.

Overall, the momentum flux or u* could be estimated successfully with the ID method (next section), and the heat fluxes will be more challenging to estimate accurately.

The time pseudo-structure functions were calculated. Their analysis is not shown here as they do not bring new information compared to what was is presented above.

4. Turbulent fluxes

As in Bourras et al. (2009), the turbulent fluxes and quantities are calculated with three methods: the ID method, the EC method and the bulk method (COARE algorithm, Fairall et al., 2003).

Here, the methodology used is to launch a first reference run of the Albatros flux calculation algorithm with common options that are: no distortion correction, application of the SC correction of the *w*-wind component of L. Baggio (Bourras et al. 2019), and no application of imbalance term on the ID method. In the COARE, the roughness length parametrization follows Smith (1988), and the options jwarm and jcool are set to zero, which means that the radiation fluxes are not accounted for in the COARE algorithm. There are several other options that are enabled and that will be described in the following section (filtering, time lag correction).

In a second time, various options are applied during the calculation, and the differences obtained with respect to the reference run are analyzed.

4.1 Friction velocity u_*

4.1.1 Reference run

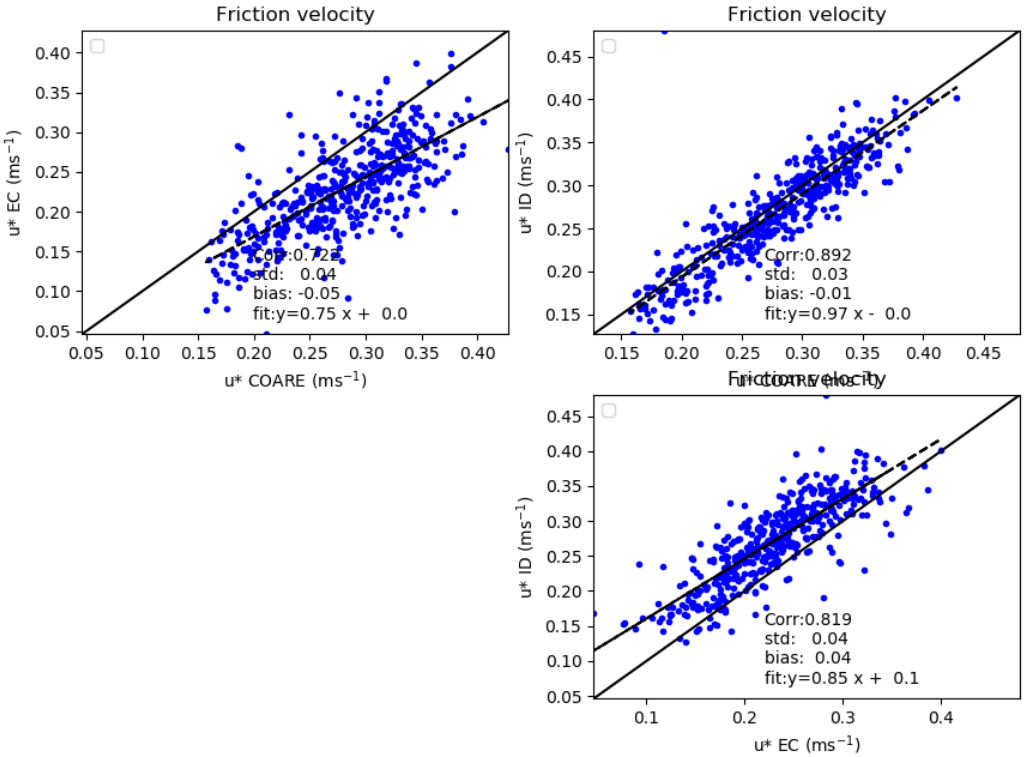

Figure 45. u* comparison, as calculated with the EC, ID and bulk methods (reference run)

The ID u* estimates have a good fit to the bulk u* values (Figure 45, upper right). Despite no imbalance term was accounted for in the Turbulent Kinetic Energy (TKE) equation, there is a negligible bias (-0.01 m/s), which contrasts with AMMA 2006 data (Bourras et al., 2009) where a -0.46 z/L imbalance had to be accounted for. The standard deviation of the difference between ID u* and bulk u* is 0.03 m/s, which is good.

The EC u* estimates are well correlated to ID u* values (rms=0.819, Figure 45 lower right), but there is a significant bias (0.04 m/s), which is indicative of a lack of energy in EC u* estimates, possibly due to wind flow distortion, and which is consistent with section 3 conclusions.

The comparison between EC u* and bulk u* estimates is degraded compared to the other comparison (Figure 45, upper left).

4.1.2 Application of the distortion correction

The application of the vertical angle correction to the mean wind does not significantly affect the results (not shown). The comparison between ID* and EC* is slightly improved, but the other comparisons are slightly degraded, as reported hereafter.

u* comparison	Correlation	σ	bias	Slope of linear fit
EC-bulk	0.674	0.05	-0.07	0.7
ID-bulk	0.894	0.03	-0.01	0.96
ID-EC	0.775	0.04	0.06	0.8

4.1.3 Correction de la vitesse verticale du vent

If the vertical wind motion is not accounted for, the comparison between EC u* and bulk u*bulk is seriously degraded, as expected according to section 3 results.

u* comparison	Correlation	σ	bias	Slope of linear fit
EC-bulk	0.178	0.09	-0.04	0.58
ID-bulk	0.892	0.03	-0.01	0.97
ID-EC	0.465	0.07	0.03	0.38

4.1.4 No filtering of EC data

In the reference run, a high-pass filter was applied to the EC time series (for cleanup), at a frequency of fz/U=0.01. It this filter is disabled, the comparisons of section4.1.1 are slightly affected. Specifically, the slope between EC u* and ID u* is decreased to 0.66. In conclusion, the filtering improves the comparisons.

u* comparison	Correlation	σ	bias	Slope of linear fit
EC-bulk	0.632	0.05	-0.05	0.75
ID-bulk	0.892	0.03	-0.01	0.97
ID-EC	0.721	0.05	0.04	0.66

4.1.5 No phase lag correction (lag velz';w' and lag w';q')

In the reference run, time lags are arbitrarily corrected. The maximum correlation is found between the time series, by gradually shifting one of the time series. The lag was searched in the following ranges, +/-200 points for velz';w' and 500 points for w';q', which correspond to 6 and 15 seconds of maximum time shift, respectively.

If the time lag correction is not accounted for, the comparison between EC u* and ID u* is slightly improved.

u* comparison	Correlation	σ	bias	Slope of linear fit
EC-bulk	0.738	0.04	-0.05	0.77
ID-bulk	0.893	0.03	-0.01	0.97
ID-EC	0.827	0.03	0.04	0.86

4.1.6 Radiation fluxes in the bulk algorithm

If jwarm=1 and jcool=1 in the bulk algorithm, the impact on the u* comparisons is negligible.

u* comparison	Correlation	σ	bias	Slope of linear fit
EC-bulk	0.725	0.04	-0.05	0.75
ID-bulk	0.893	0.03	-0.01	0.97
ID-EC	0.819	0.04	0.04	0.86

4.2 Latent heat flux

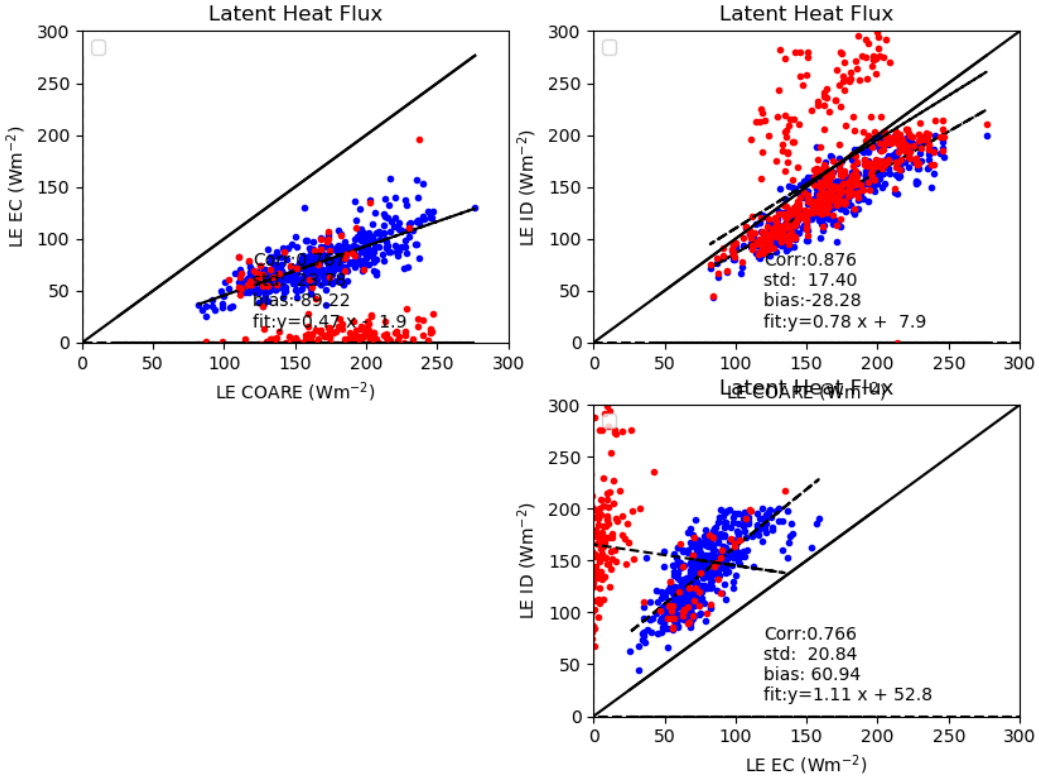

Figure 46. LE comparison, calculated with the EC, ID and bulk methods (reference run). Refractometer data are plotted in blue, while LICOR data are plotted in red.

There is a good agreement between ID LE and bulk LE in correlation (0.876) and standard deviation of the difference (σ = 17.4 W/m2), as shown in Figure 46. Unfortunately, there is a large bias (-28.8 W/m2) for refractometer data, and the slope of linear fit is far from unity (0.78). This behavior of ID LE estimates was already observed during AMMA 2006 (Bourras et al., 2009).

Most of the EC LE estimates have almost null values, which is attributed to the lack of time coherence between Gill and LICOR data, as anticipated in section 3 with the analysis of the co-spectra.

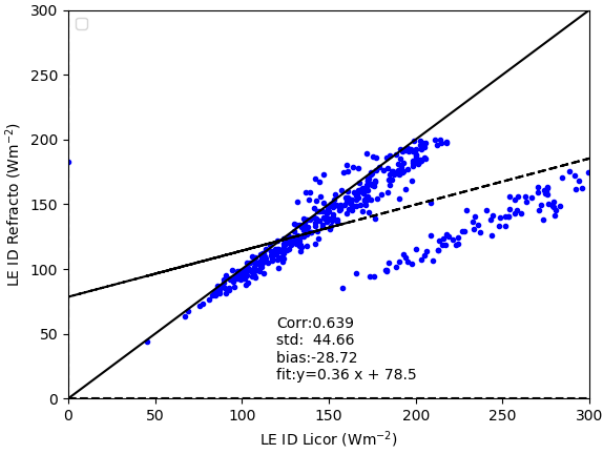

Figure 47. Comparison between LICOR and refractometer ID LE estimates

A further comparison of Refractometer ID LE estimates to LICOR ID LE estimates reveals that, apart for a group of outlier points, there is a systematic deviation of + 10 W/m2 (LICOR estimates are larger than the refractometer estimates), as shown in Figure 47. The same bias was already observed with the AMMA 2006 data.

In Figures 46 and 47, it is encouraging to note that LICOR and refractometer ID LE estimates have a good correlation and standard deviation of the difference (except for the outlier points). It suggests that the underestimation of the ID LE estimates compared to bulk LE estimates is confirmed by two independent instruments.

4.3 Buoyancy flux

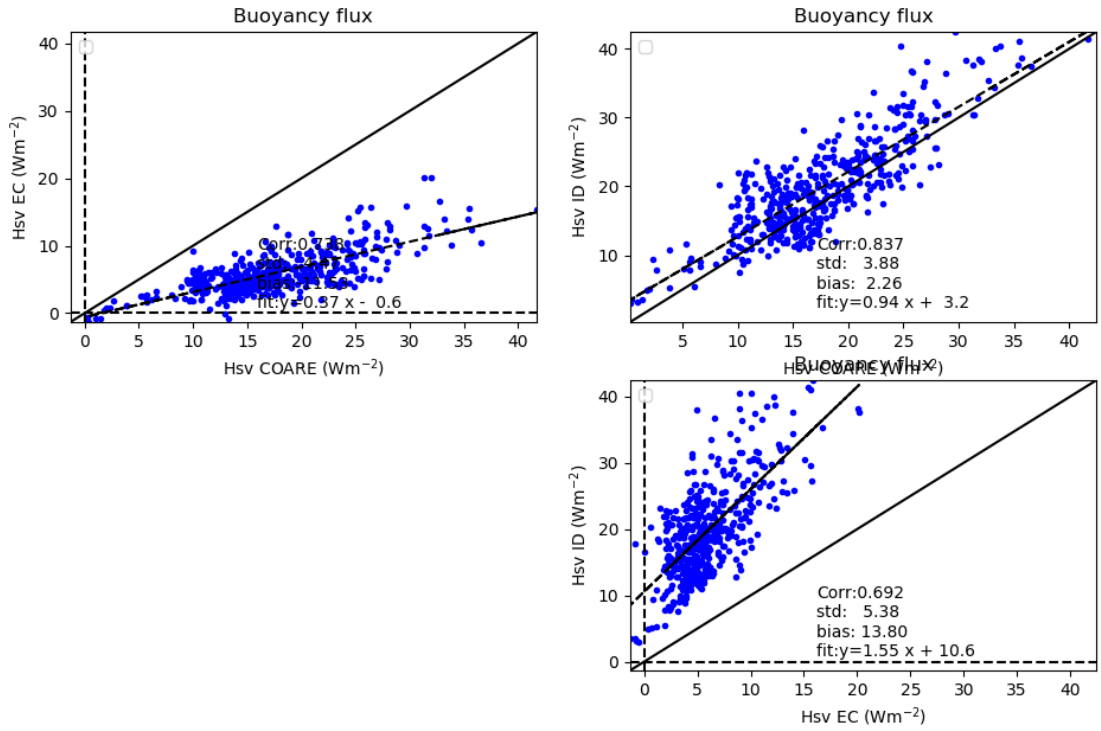

Figure 48. Comparisons for the buoyancy fluxes

The comparison between ID HSv and bulk HS is satisfying (Figure 48), which is not the case for the comparison to EC HSv estimates.

With radiation fluxes enabled (jwarm=jcool=1) in the bulk algorithm, the comparison between ID HSv and Bulk HSv is slightly degraded, except in terms of slope of linear fit. As a result, the use of the radiation option in the bulk algorithm may be discussed.

HSv comparison	Correlation	σ	bias	Slope of linear fit
ID-bulk	0.838	3.85	4.99	1.03

4.4 Sensible heat flux

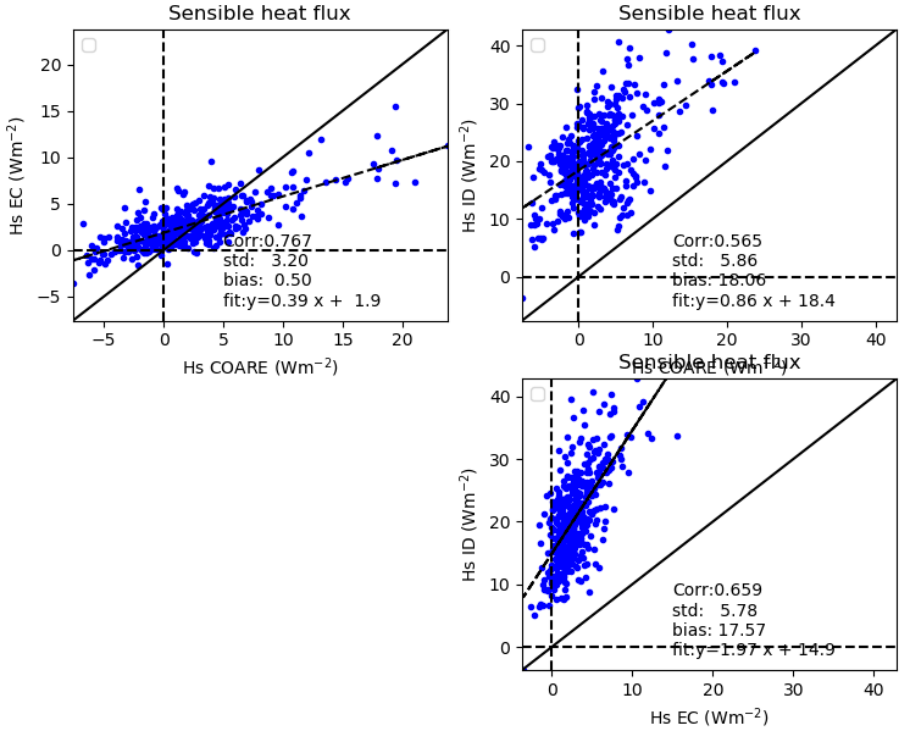

Figure 49. Comparisons for the sensible fluxes

As expected, because of the large biases in LE comparisons (section 4.2), the comparisons are disappointing for the sensible heat flux (Figure 49). In doubt, the bulk values are used in the following for producing the flux data set.

4.5 Comparison to OCARINA fluxes

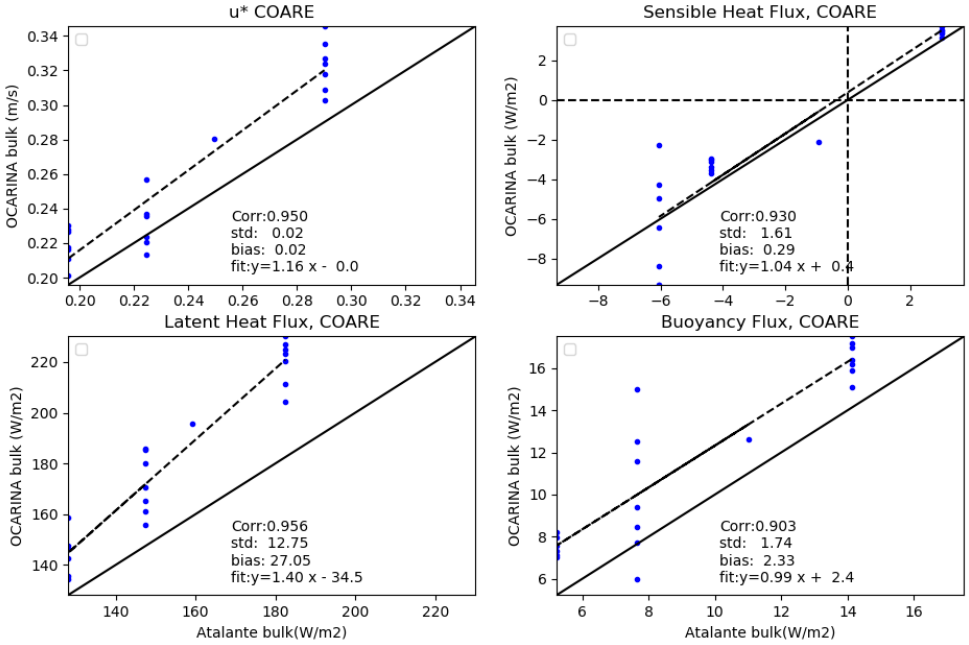

Figure 50. Comparison between Atalante and OCARINA bulk turbulent fluxes

Please note, as in section 2.4, that very few points of comparisons are available. Despite this, the coefficients of correlation of the comparisons are encouraging, as they are all larger than 0.9 (Figure 50).

The Atalante u* values are underestimated with respect to OCARINA data (bias=-0.02 m/s and slope of OCARINA minus Atalante equal to 1.16). This is consistent with the U10N difference observed in section 2.4

The sensible and buoyancy fluxes have a good statistical agreement, with biases and standard deviation of error within 2 W/m2.

The OCARINA LE values are largely overestimated with respect to Atalante LE values, by +27 W/m2, and the slope of linear fit is way larger than unity (1.4). This confirms that the accurate estimation of the latent heat flux is problematic for EUREC4A data.

5. EUREC4A flux data set

In this section, we present the time series and the statistical elements for the reference run (variables and fluxes). The turbulent fluxes considered are the bulk fluxes.

Variable	Unit	Mean value	RMS deviation	Minimum	Maximum
Incoming Solar flux (positive)	(W/m2)	248.92	325.74	-4.51	956.97
Upward solar flux (positive)	(W/m2)	14.94	19.54	-0.27	57.42
Downward infrared flux (positive)	(W/m2)	419.95	13.33	386.64	475.80
Upward infrared flux (positive)	(W/m2)	455.29	1.65	449.13	458.33
Net shortwave flux	(W/m2)	233.99	306.20	-4.24	899.55
Net longwave flux	(W/m2)	-35.34	13.23	-69.74	19.42
Net radiation flux	(W/m2)	198.65	307.09	-71.68	860.91
Turbulent sensible heat flux	(W/m2)	-4.21	4.86	-27.43	7.18
Turbulent latent heat flux	(W/m2)	-174.49	38.09	-278.59	-80.43
Surface heat budget	(W/m2)	**19.95**	315.01	-333.54	770.97
Wind speed @ 17 m	(m/s)	8.15	1.45	4.01	11.88
Sea surface temperature	(°C)	27.32	0.27	26.30	27.82
Air temperature @ 17 m	(°C)	26.78	0.43	24.43	27.50
Surface specific humidity	(g/kg)	22.26	0.37	20.88	22.94
Air specific humidity @ 17 m	(g/kg)	15.55	0.82	13.18	17.35
Atmospheric pressure @ 17 m	(hPa)	1012.49	1.49	1008.42	1016.42
Turbulent friction velocity	(m/s)	0.28	0.05	0.13	0.44
Monin-Obukhov ratio	(no unit)	-0.17	0.12	-1.25	-0.00
Wind stress	(N/m2)	**0.09**	0.04	0.02	0.22
10 m-neutral wind speed	(m/s)	8.06	1.35	4.24	11.54
10 m-neutral air temperature	(°C)	26.92	0.45	24.18	27.65
10 m-neutral specific humidity	(g/kg)	15.43	0.85	12.91	17.17

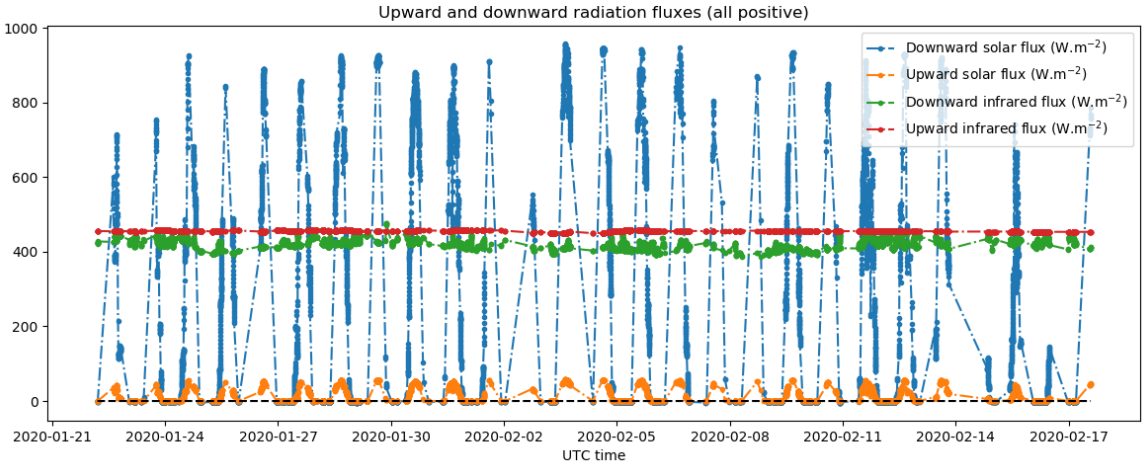
Upward and downward radiation fluxes (all positive)
Downward solar flux (W.m^{-2})
Upward solar flux (W.m^{-2})
Downward infrared flux (W.m^{-2})
Upward infrared flux (W.m^{-2})
1000
800
600
400
200
0
2020-01-21
2020-01-24
2020-01-27
2020-01-30
2020-02-02
2020-02-05
2020-02-08
2020-02-11
2020-02-14
2020-02-17
UTC time

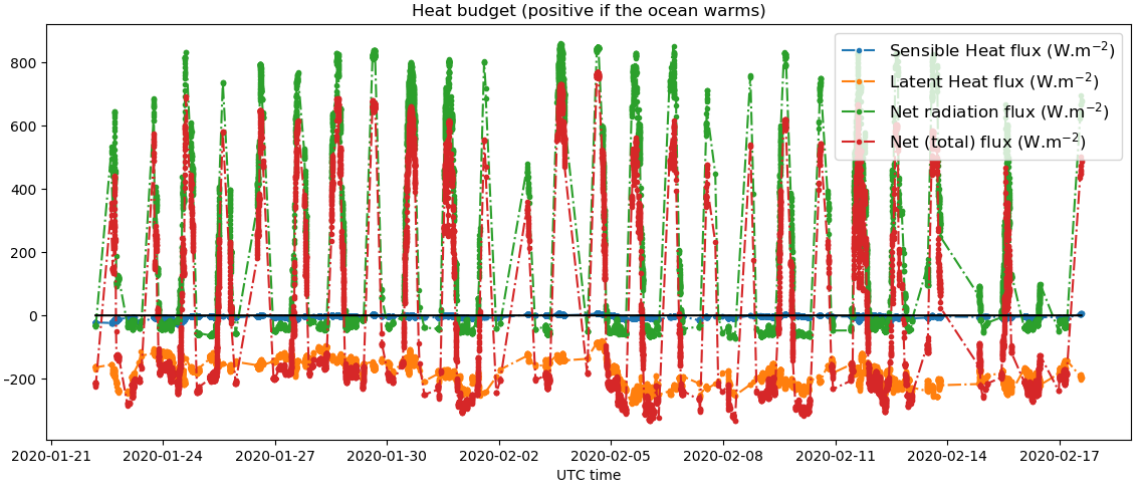
Heat budget (positive if the ocean warms)
Sensible Heat flux (W.m^{-2})
Latent Heat flux (W.m^{-2})
Net radiation flux (W.m^{-2})
Net (total) flux (W.m^{-2})
800
600
400
200
0
-200
2020-01-21
2020-01-24
2020-01-27
2020-01-30
2020-02-02
2020-02-05
2020-02-08
2020-02-11
2020-02-14
2020-02-17
UTC time

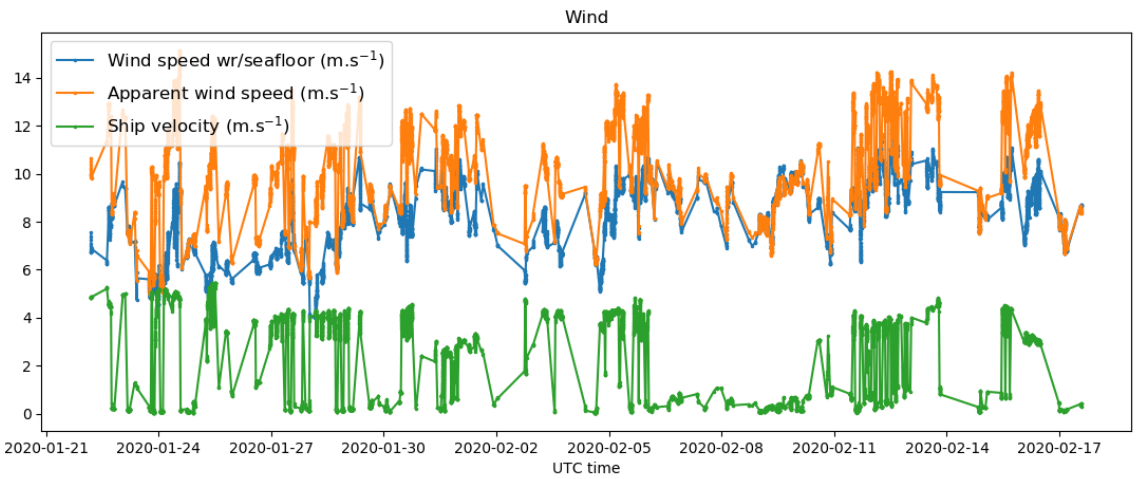
Wind
Wind speed wr/seafloor (m.s^{-1})
Apparent wind speed (m.s^{-1})
Ship velocity (m.s^{-1})
14
12
10
8
6
4
2
0
2020-01-21
2020-01-24
2020-01-27
2020-01-30
2020-02-02
2020-02-05
2020-02-08
2020-02-11
2020-02-14
2020-02-17
UTC time

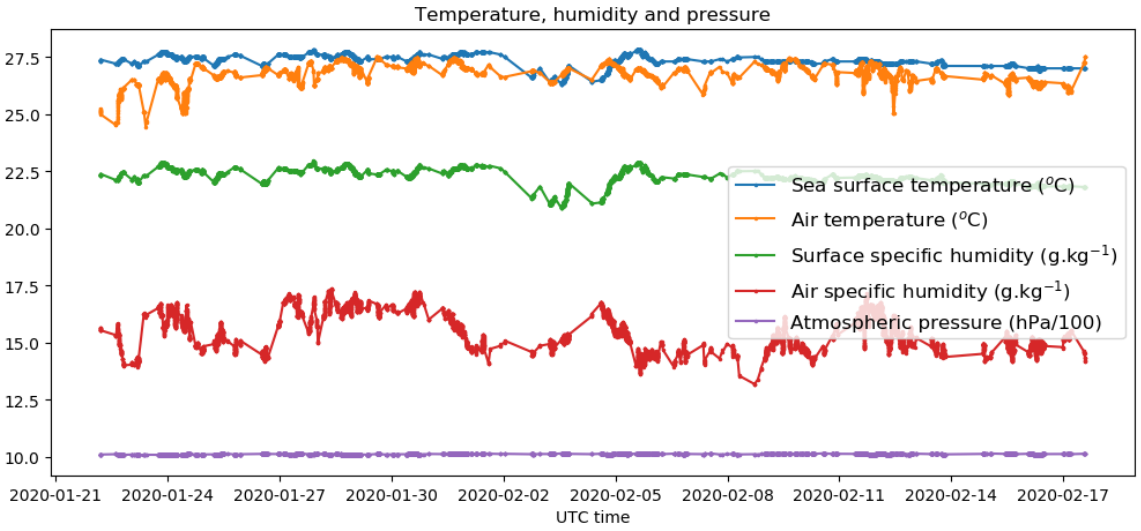
Temperature, humidity and pressure
Sea surface temperature (°C)
Air temperature (°C)
Surface specific humidity (g.kg^{-1})
Air specific humidity (g.kg^{-1})
Atmospheric pressure (hPa/100)
UTC time

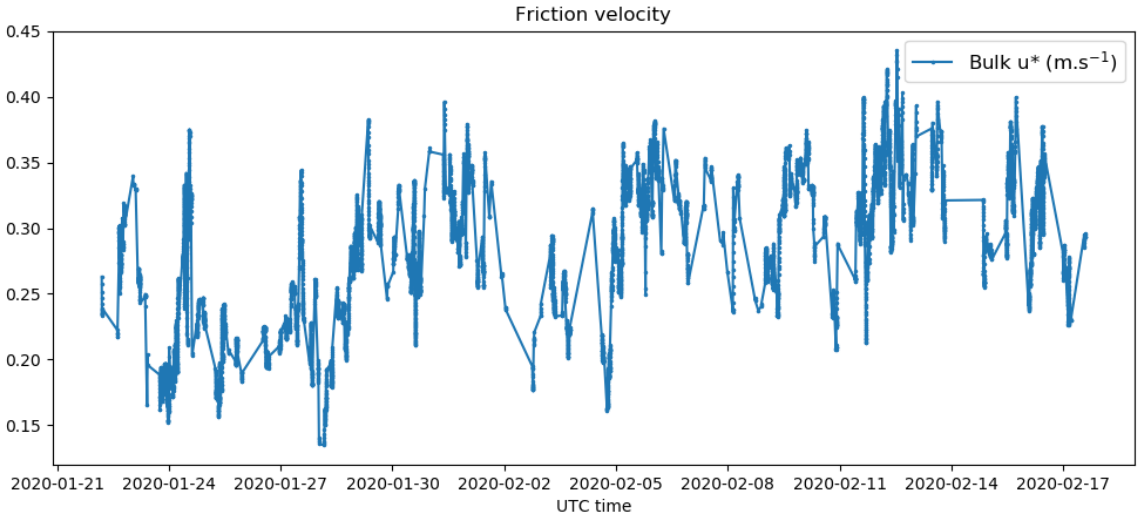
Friction velocity
Bulk u* (m.s^{-1})
UTC time

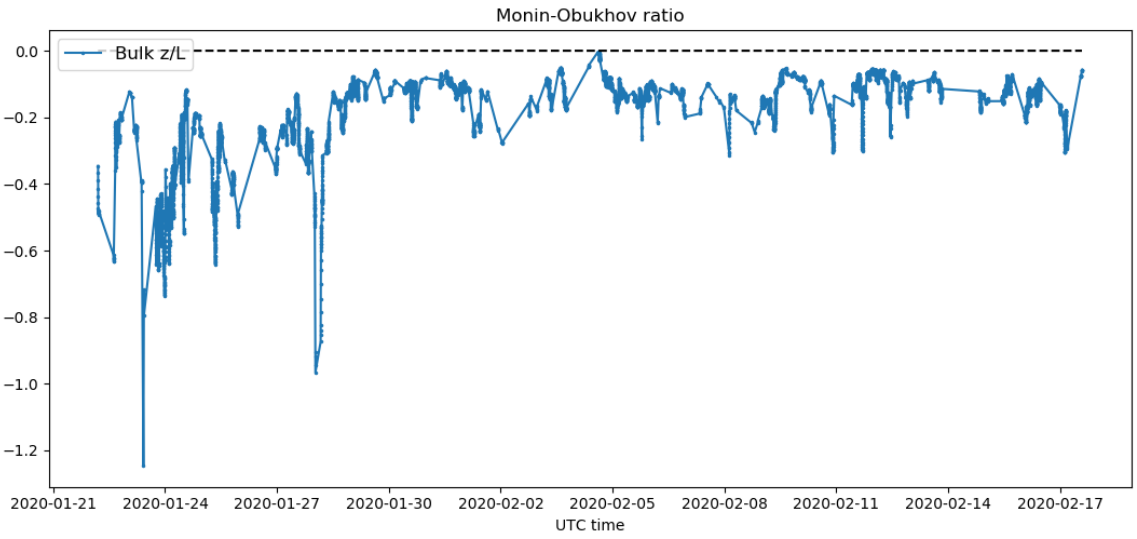
Monin-Obukhov ratio
Bulk z/L
UTC time

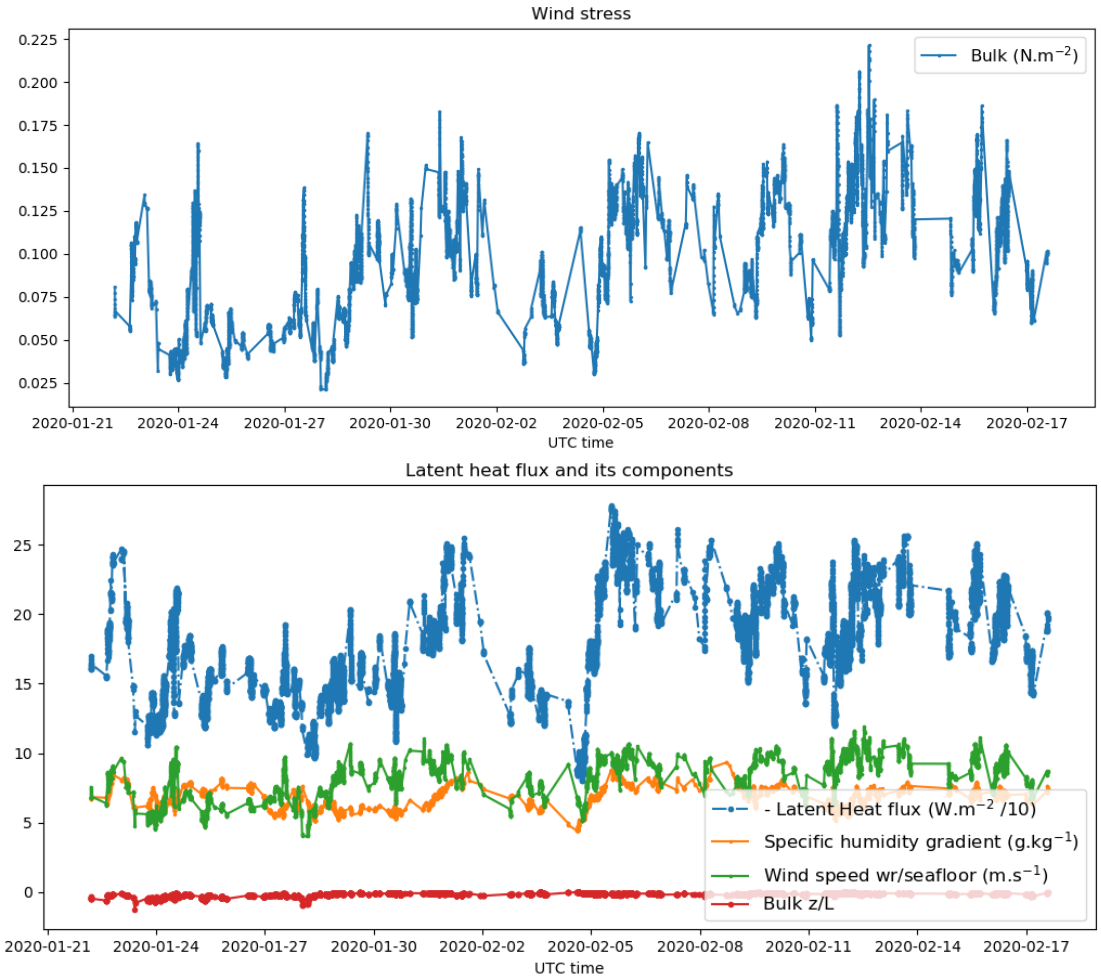

List of variables in the flux dataset:

Name of variable	Variable	Example value	Standard Unit	Long name
lon	Longitude	-59.160592	degrees_east	In decimal degrees
lat	Latitude	12.780028	degrees_north	In decimal degrees
pair	Atmospheric pressure	1010.60	hPa	Atmospheric pressure at 17 m
tair	Air temperature	25.28	degC	Air temperature at 17 m
rho	Air density	1.168	kg m-3	Air density at 17 m
hur	Relative humidity of air	0.78	1	Relative humidity at 17 m
sst	Sea surface temperature	27.304	degC	SST from R/V sensor
rlds	Downwelling infrared flux	416.6	W m-2	Downwelling longwave radiation flux, positive

				downward
rlus	Upwelling infrared flux	455.2	W m-2	Upwelling longwave radiation flux, positive upward
rsds	Downwelling solar flux	-1.2	W m-2	Downwelling shortwave radiation flux, positive downward
rsus	Upwelling solar flux	-0.1	W m-2	Upwelling shortwave radiation flux, positive upward
wspd	Measured wind speed	7.93	m s-1	Magnitude of wind velocity with respect to ground, at a height of 17 m
u10n	10 m-neutral wind speed	8.02	m s-1	Equivalent neutral wind extrapolated at a 10-m height, from bulk calculation
t10n		25.35	degC	Equivalent neutral air temperature extrapolated at a 10-m height, from bulk calculation
q10n		15.34	g kg-1	Equivalent neutral air specific humidity extrapolated at a 10-m height, from bulk calculation
ustar_bulk	Friction velocity	0.28	m s-1	Bulk turbulent surface friction velocity, COARE 3.0 (please see header), zo parameterization from Smith (1988)
hsv_bulk	Buoyancy flux	33.80	W m-2	Bulk turbulent surface buoyancy flux, positive upward, from bulk calculation
hfss_bulk	Sensible heat flux	20.43	W m-2	Bulk turbulent surface sensible heat flux, positive upward, from

				bulk calculation
hfls_bulk	Latent heat flux	176.00	W m-2	Bulk turbulent surface latent heat flux, positive upward, from bulk calculation
zL_bulk	Monin Obukhov ratio	-0.301	1	Monin-Obukhov ratio, which quantifies surface boundary layer stability, from bulk calculation

6. Conclusions

The comparison to OCARINA data suggests that:

- The Atalante u* values are possibly underestimated by 0.02 m/s. It is suspected that the airflow slows down at the level of the flux mast.
- The estimation of the bulk latent heat flux has a large uncertainty of +/-30W/m2

The EC fluxes are not accurate and are generally underestimated compared to the bulk or ID LE estimates. This is possibly explained by the position of the flux mast which damps the turbulent fluctuations. For future campaigns, the mast should be placed at the bow of the ship (which was already suspected in Bourras et al., 2009).

As the EUREC4A EC data lack of accuracy, they cannot be used to improve or contest the existing bulk parameterizations of the exchange coefficients or of the roughness lengths for wind, temperature or humidity.

LICOR data are problematic to use because of issues with time drift in data. However, LICOR and refractometer ID LE values have a good fit to each other in terms of correlation coefficient and standard deviation of the difference (20 W/m2). The LICOR ID LE values are larger than the refractometer estimates by 10 W/m2, as already observed in Bourras et al. (2009).

Humidity is challenging to measure during EUREC4A. This should be seriously addressed for the upcoming experiments. Specifically,

- The humidity instruments should go back to manufacturers for calibration (WXT Atalante, LICOR, and WXT OCARINA). In addition, the LICOR temperature and air pressure data are doubtful.
- The humidity data from the different instruments should be further compared in situ (WXT and LICOR)
- The humidity from EUREC4A, AMMA 2006 and AMOP 2014 past campaigns should be further analyzed. It would help elucidate the issues with the position of the mast, with the estimation of humidity and of the latent heat flux. The following issues have to be addressed:
    - Under estimation of ID LE estimates compared to bulk LE values

- Possible modification of the Corrsin constant for humidity

The imbalance term of 0.46 z/L of the TKE equation used in Bourras et al. (2009) is not required for EUREC4A ID data, which should be further investigated.

More points of comparison between Atalante and OCARINA data should be obtained for future campaigns. For EUREC4A, the four available OCARINA deployments are insufficient.

The LICOR CO2 data were not considered in this document, but they are available upon request.

The -5/3 slope is not respected for temperature, as it is systematically observed for all campaigns. This issue must be further addressed.

The synchronization of LICOR time data should be reworked. As the acquisition system is configured now, it is impossible to synchronize LICOR data to other instrument data.

Some Gill data are systematically missing in the recorded files, and are dated according to PC-flux data. The acquisition system is not fully satisfying as it is presently configured.

7. References

Bourras, D., Weill, A., Caniaux, G., Eymard, L., Bourlès, B., Letourneur, S., Legain, D., Key, E. L, et al. (2009). Turbulent air-sea fluxes in the Gulf of Guinea during the AMMA Experiment. Journal of Geophysical Research: Oceans, 114, C04014. https://doi.org/10.1029/2008JC004951

Bourras, D., Branger, H., Reverdin G., Marié, L., Cambra, R., Baggio, L., Caudoux, C., Caudal, G., et al. (2014). A new platform for the determination of Air-sea Fluxes (OCARINA): overview and first results. Journal of Atmospheric and Oceanic Technology, 31, 1043–1062. https://doi.org/10.1175/JTECH-D-13-00055.1

Bourras Denis, Cambra Remi, Marié Louis, Bouin Marie-Noëlle, Baggio Lucio, Branger Hubert, Beghoura Houda, Reverdin Gilles, Dewitte Boris, Paulmier Aurélien, Maes Christophe, Ardhuin Fabrice, Pairaud Ivane, Fraunié Philippe, Luneau Christopher, Hauser Danièle (2019). Air-Sea Turbulent Fluxes From a Wave-Following Platform During Six Experiments at Sea. Journal Of Geophysical Research-oceans, 124(6), 4290-4321. Publisher's official version : https://doi.org/10.1029/2018JC014803 , Open Access version : https://archimer.ifremer.fr/doc/00503/61436/

Delahaye, J. Y., C. Guerin, J. P. Vinson, H. Dupuis, A. Weill, H. Branger, L. Eymard, J. Lavergnat and G. Lachaud (2001), A new shipborne microwave refractometer for estimating the evaporation flux at the sea surface, J. Atmos. Oceanic Technol., 18, 459-475.

Dupuis, H., Taylor, P. K., Weill, A., & Katsaros, K. (1997). Inertial dissipation method applied to derive turbulent fluxes over the ocean during the Surface of the Ocean, Fluxes and Interactions with the Atmosphere/Atlantic Stratocumulus Transition Experiment (SOFIA/ASTEX) and Structure des Echanges Mer-Atmosphere, Propriétés des Hétérogénéités Océaniques: Recherche Expérimentale (SEMAPHORE) experiments with low to moderate wind speeds. *Journal of Geophysical Research: Oceans*, 102(C9), 21115–21129. https://doi.org/10.1029/97JC00446

Fairall. C. W., Bradley, E. F., Hare, J. E., Grachev, A. A., & Edson, J. B. (2003). Bulk Parameterisations of Air-Sea Fluxes: Updates and Verification for the COARE Algorithm. Journal of Climate, 16, 571-591. https://doi.org/10.1175/1520-0442(2003)016%3C0571:BPOASF%3E2.0.CO;2

Geyskens, N. (2020). Radiosounding EUREC4A-OA Report, R/V Atalante, 16 pages, in French (available on request).

Kaimal, J. C., Wyngaard, J. C., Izumi, Y., & Coté, O. R. (1972). Spectral Characteristics of surface-layer turbulence. Quarterly Journal of the Royal Meteorological Society, 98, 563-589. https://doi.org/10.1002/qj.49709841707

Pedreros, R., Dardier, G., Dupuis, H., Graber, H. C., Drennan, W. M., Weill, A., Guérin, C., & Nacass, P. (2003). Momentum and heat fluxes via the eddy correlation method on the R/V L'Atalante and an ASIS buoy. *Journal of Geophysical Research: Oceans*, 108(C11), 3339. https://doi.org/10.1029/2002JC001449

Smith, S. D. (1988). Coefficients for sea surface wind stress, heat flux, and wind profiles as a function of wind speed and temperature. *Journal of Geophysical Research: Oceans*, 93(C12), 15467–15472. https://doi.org/10.1029/JC093iC12p15467